Korean J. Chem. Eng., 40(3), 675-692 (2023)
DOI: 10.1007/s11814-022-1223-z

pISSN: 0256-1115
eISSN: 1975-7220

Enhanced CO_2/N_2 separation performance in HP-Cu-BTCs by modifying the open-metal sites and porosity using added templates

Ping Yang*, Rujin Zhou*, Youhua Zhang*, Shui Cao*, Dan Zhang*, Hongbing Ji, Linhai Duan*,†, and Xiuhong Meng*,†**

*Key Laboratory of Inferior Crude Oil Processing of Guangdong Provincial Higher Education Institutes, Guangdong University of Petrochemical Technology, Maoming 525000, P. R China
**The Key Laboratory of Low-Carbon Chemistry & Energy Conservation of Guangdong Province, Sun Yat-Sen University, Guangzhou 510275, P. R. China
(*Received 6 May 2022 • Revised 23 June 2022 • Accepted 4 July 2022*)

Abstract−HP-Cu-BTCs (CTAB), HP-Cu-BTC(N,N), HP-Cu-BTC(SDBS) series with open metal coordination site Cu(I), cage window sites, tunable porosity, high specific surface area, cavity, etc., were synthesized using cationic surfactant (cetyltrimethylammonium bromide, neutral organic amine, and an anionic surfactant as templates, respectively, A variety of techniques were used to analyze the materials before and after CO_2 cycle adsorption at 303 K. A high BET specific surface area (1,194.06 m^2/g) and total pore volume (0.63 cm^3/g) were found in the synthesized HP-Cu-BTC(N,N). The synthesized HP-Cu-BTC(N,N) not only has high CO_2 adsorption capacity (7.4293 mmol/g) but also good selectivity (37.20) for adsorption separation of CO_2/N_2. Besides, FT-IR spectroscopy, CO_2-TPD curves and adsorption kinetic curve demonstrated that the adsorption mechanism of synthesized HP-Cu-BTC(N,N) was mainly attributable to physisorption and it could be regenerated at relatively low temperature. The mesoporous structure not only improves the uptake capacity but also improves the diffusion and mass transfer of CO_2. At the same time, the CO_2-TPD showed that the HP-Cu-BTCs may have two major adsorption sites. One is to absorb CO_2 molecules through van der Waals forces. The other is the electrostatic interaction of the open Cu sites with CO_2. Therefore, the CO_2/N_2 adsorption selectivity of HP-Cu-BTC(N,N) is significantly higher than that of conventional Cu-BTC. After five consecutive adsorption/desorption cycles, the adsorbents retained an excellent adsorption property. Thus, it is a very good adsorbent for the CO_2 capture.

Keywords: CO_2 Adsorption, Hierarchical Porous Cu-BTC, Template, Metal Effect, Isosteric Heat of Adsorption, Regenerability

INTRODUCTION

The release of CO_2 into the atmosphere by the burning of fossil fuels is the primary source of the global climate change phenomena [1,2]. Over the last 200 years, fossil fuels have historically been utilized in massive volumes to power human civilization, and now fossil fuel combustion meets over 85 percent of global energy demand. The intrinsic energy density, quantity, and economic reliance of contemporary civilization on their purchase and trading are the causes for our lopsided reliance on fossil fuels as our major energy source. Global energy consumption is rapidly increasing, which is causing serious environmental issues. Concerns about the possible influence of CO_2 emissions from fossil fuel burning on global climate change have prompted a slew of CO_2 reduction measures [3-7]. CO_2 is a significant C1 resource and chemical raw material in addition to being a greenhouse gas. The development of new technologies to convert CO_2 into chemical raw materials will aid in the optimization of the future society's energy structure. As a result, high-efficiency CO_2 separation is required, which is a necessity for CO_2 usage in the future.

Although it is unrealistic to totally eliminate CO_2 emissions, it is feasible to reduce them by using effective separation technology. Post-combustion (flue gas from power production), pre-combustion (fossil fuels), and oxygen-enriched combustion separation technology are the three primary types of carbon capture and storage (CCS) technology [8,9]. Pre-combustion CO_2 capture entails enriching and separating CO_2 and other components of fossil fuels prior to combustion. To achieve efficient, low-carbon green energy conversion, this technology is planned to be used with integrated gasification combined cycle power plants. The burning of fossil fuels in an oxygen-enriched atmosphere with flue gas circulation is referred to as oxygen-enriched combustion. CO_2 and H_2O are the major components of flue gas produced by this method. At the moment, the most extensively utilized method is post-burning removal, which involves using gas separation technology to separate and collect CO_2 from a gas source after combustion. Physical adsorption, chemical adsorption, and membrane separation have all drawn the interest of scientists from many fields [2,10,11]. Membrane separation, on the other hand, is difficult to use in industrial settings owing to its exorbitant price. Absorption of chemicals using amine-solution systems has a number of drawbacks, including rusting of equipment and a highly energetic need for CO_2 collecting. Adsorption via physical means using porous solids as adsorbents, on the other hand, is frequently utilized in CO_2 collection because of its

†To whom correspondence should be addressed.
E-mail: lhduan@126.com, mengxiuh@163.com
Copyright by The Korean Institute of Chemical Engineers.

environmental friendliness and economic feasibility. For CO_2 adsorption, many porous solid adsorbents have been developed, including metalorganic frameworks (MOFs) and zeolites (as well as other porous materials) [12-15]. When compared to other porous materials, MOFs with adjustable physical properties, amazing porosity, and superb crystallinity function very well as CO_2 adsorbents [16-18].

Metal-organic frameworks (MOFs) have paved the way for the creation of novel materials. Likewise, research on MOFs is motivated by virtue of their astounding compositional and structural variety, long-term porosity, very low density, and well delineated pores and channels. The large interior surface area of MOFs is a key characteristic that has been shown to be extremely desired in a variety of possible applications, comprising the storage of hydrogen, the purification of natural gas, the improvement of biogas, and CO_2 and N_2 separation [19]. Along with the necessity for CO_2 capture capacity, the adsorbent's stability through repeated CO_2 capture cycles (i.e., adsorption/desorption) must be addressed [20-22].

Cu-BTC, one of the most commonly reported MOFs consisting of low-cost basic materials [23,24], is one of the most frequently reported, is simple to synthesize, has a large specific surface area, is thermally stable, and typically includes fresh air, with visitors having access to 60% of the capacity [25,26]. Additionally, it exhibits superior CO_2 adsorption, selectivity, and regeneration properties when used in conjunction with precise adsorption and desorption conditions. Cu-BTC is made up of Cu_2O units that are connected by linear benzene-1,3,5-tricarboxylic acid (BTC). An alternative spacer is used in lieu of the BTC molecule. It maintains the net's inherent properties while offering a well-designed interface for adjusting the pore size and functioning of the framework [27]. Additional binding sites for guest gas molecules may be provided by the partial positive charges that are present on the copper metal sites in Cu-BTC. This is critical for the adsorption of tiny molecules such as hydrogen and for increasing the selectivity of adsorption for separating mixtures including molecules with various polarities, particularly at low pressures. Cu-BTC is a three-dimensional network with intersectional pores, a 0.6 nm tetrahedral side pocket, and a 1.0-1.2 nm cage/window cage. The tetrahedral pockets and major channels are joined by triangular windows of 0.35 nm diameter [28-31], precisely the dimension required to segregate CO_2 (shapes/sizes $3.2\times3.3\times5.4$ Å^3 and kinetic diameters of ~3.3 Å) and N_2 (kinetic diameter: 3.64 Å) [32,33]. The sole kink in the ointment is that the pure microporous regime (pore size <2 nm) of Cu-BTC restricts adsorbate diffusion, which reduces CO_2 interaction with the Cu-BTC pore walls [34]. Additionally, the inclusion of mesoporous structures increases the pore volume of the hierarchical porous MOFs material, resulting in a better adsorption capacity [35]. Hierarchical porous materials, in particular, allow for easy regulation of their structure and function at the atomic or molecular level [36]. As a result, their success is crucial in developing a reliable method for converting microporous MOFs to hierarchical porous counterparts with micropores and mesopores [37].

So far, eight distinct strategies for increasing the pore size of traditional MOFs have been developed: ligand extension [38], post-processing [39], mixed ligands [40], templating [41], control synthesis conditions [42-44], ionic liquid, and [45] modulator-induced defect-formation technique [46-48]. However, in HP-MOF products produced through the ligand extension approach, lower mesopore sizes (<10 nm), volatility, insecurity, and frail interconnected frameworks are nearly inescapable [49]. Additionally, post-processing and mixed-ligand approaches often result in the formation of mesopores of uncontrolled size in the final HP-MOFs [50]. Synthetic condition control method is difficult to achieve accurate control of synthetic conditions, resulting in uneven mesoporous pores of the product and difficult to adjust the pore size. The types of ionic liquids used to synthesize hierarchically porous MOFs are limited. The composite method is difficult to organically combine microporous MOFs with functional porous materials; there are not many types of modulators for the modulation-inducing defect-forming strategy [51-53]. In comparison to the other approaches, the template method is the preferred way to synthesize of hierarchical Cu-BTC (HP-Cu-BTC) owing to the wide range of template agents and ease of operation. The inclusion of template agents significantly increased the micropore volume compared to Cu-BTC. For example, it has been reported that cetyltrimethylammonium bromide (CTAB) may be employed as a template for the synthesis of viable hierarchical porous Cu-BTC [54]. N,N-dimethylhexadecylamine and N,N-dimethyltetradecylamine have both been employed as templates for the synthesis of stable HP-MOFs (e.g., Cu-BTC) [55]. Other novel templates for the synthesis of HP-MOFs have been described, including sodium dodecylbenzene sulfonate (SDBS) [56], N-ethyl per-uorooctylsulfonamide (N-EtOFSA) [57], and 4-(dodecyloxy)benzoic acid (DBA) [58].

This study used three surfactants as templates-cationic (CTAB), neutral organic amine (N,N-dimethyltetradecylamine) and anionic (SDBS)-to establish a solvothermal approach to manufacture three stable HP-Cu-BTC(CTAB), HP-Cu-BTC(N,N) and HP-Cu-BTC (SDBS). The resultant HP-Cu-BTCs were next described and their CO_2 and N_2 adsorption isotherms were determined volumetrically at 273 K, 298 K, and 303 K at pressures ranging from 0 to 100 kPa. X-ray diffraction, FT-IR spectroscopy, and thermal analysis were used to estimate the structural stability of HP-Cu-BTCs before and after CO_2 cycle adsorption. The isosteric heat of adsorption and selectivity were determined using experimental adsorption isotherms. CO_2-TPD investigated the primary adsorption sites and adsorption conditions in HP-Cu-BTCs. In addition, we investigated the regeneration and stability of HP-Cu-BTCs in CO_2/N_2 separation using a breakthrough curve based on a fixed bed reactor, as well as their regeneration and stability across five consecutive cycles.

RESULTS AND DISCUSSION

1. Characterization of Samples

The results from XRD, FT-IR, and TG were analyzed to determine the CO_2 adsorption process on HP-Cu-BTCs. The structure of the adsorbents was studied using the XRD technique after CO_2 cycle adsorption at 303 K and 0-100 kPa. Fig. 1(a) shows the XRD patterns of all materials examined before and after CO_2 cycle adsorption. Three HP-Cu-BTCs exhibit an XRD pattern consistent with our earlier work and published data [30,59]. After CO_2 cycle adsorption, there are no changes in the positions of the peaks for

all the HP-Cu-BTCs, indicating that the framework structure is well retained. There are very minor variations in the peak intensity after CO_2 cycle adsorption. While the intensity reduces significantly following CO_2 cycle adsorption for HP-Cu-BTC(CTAB) and HP-Cu-BTC(N,N), the intensity increases for HP-Cu-BTC(SDBS). Nevertheless, at low/atmospheric pressure at 303 K, CO_2 adsorption had little effect on the architectures of all HP-Cu-BTCs.

FT-IR and TG were employed to assess the changes in surface chemistry of our samples after CO_2 cycle adsorption. Fig. 1(b) and Table S1 show the FT-IR spectra of all samples taken before and after CO_2 cycle adsorption. All of the bands were assigned in the same way as the parent Cu-BTC [60], indicating that the HP-Cu-BTCs were effectively synthesized. The large broad band seen over the range of 3,000-3,700 cm^{-1} is assigned to the O-H stretching vibration of loosely bound water molecules in HP-Cu-BTC, while the peaks around 3,427 cm^{-1} are attributed to typical O-H vibrations,

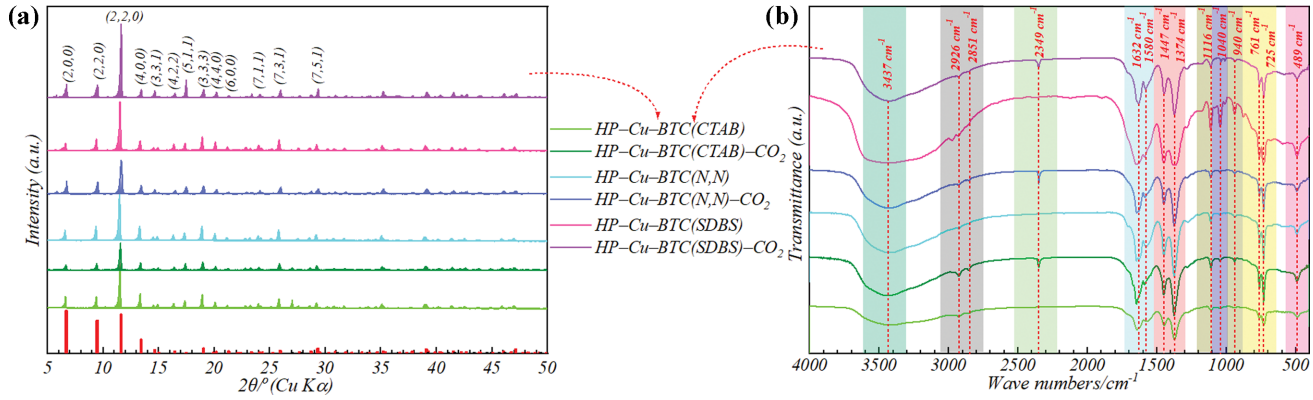


Fig. 1. (a) XRD patterns and (b) FT-IR spectra of the samples studied before and after CO_2 cycle adsorption.

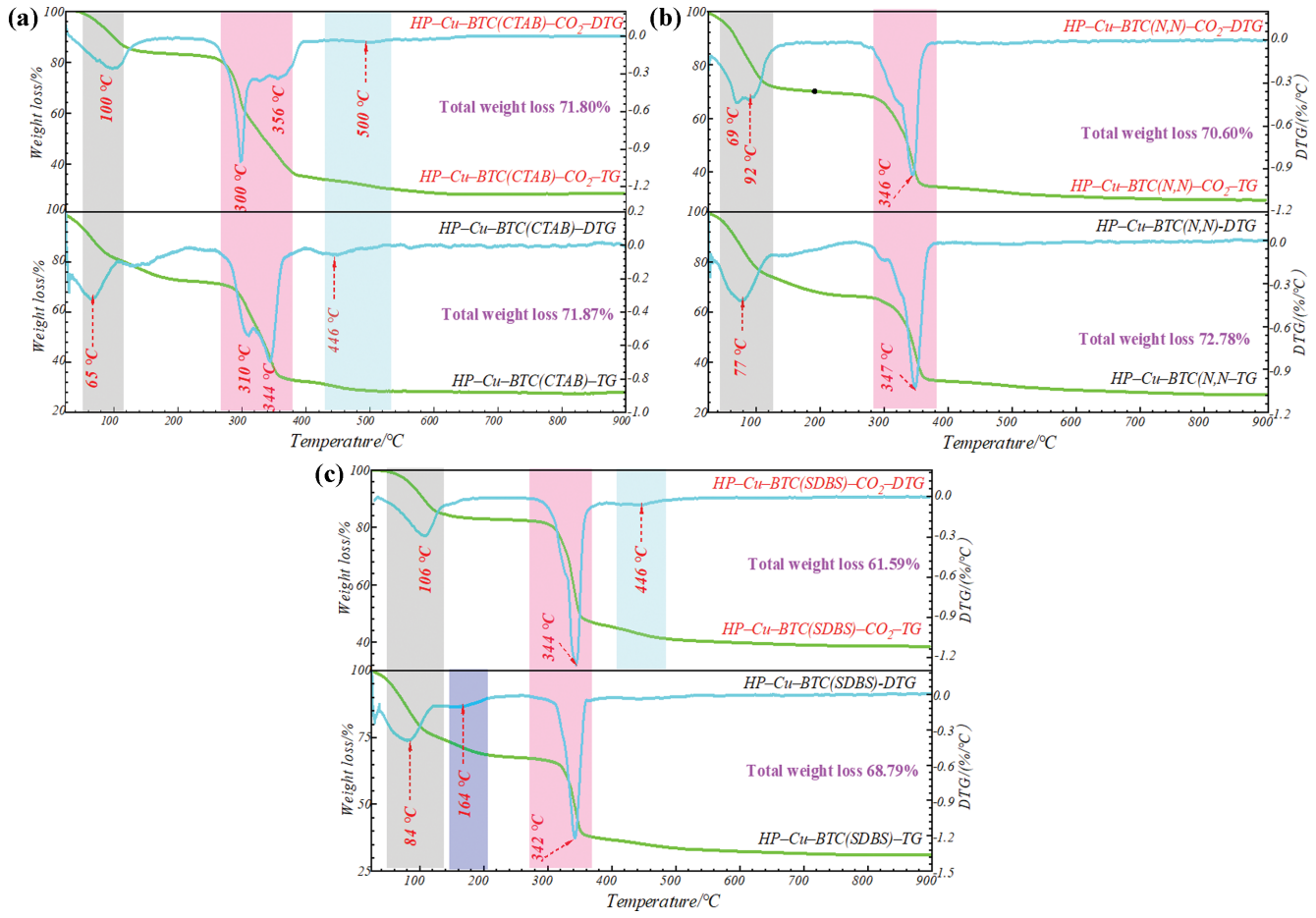


Fig. 2. TG (green) and DTG (blue) curves of the (a) HP-Cu-BTC(CTAB), (b) HP-Cu-BTC(N,N) and (c) HP-Cu-BTC(SDBS) studied before and after CO_2 cycle adsorption.

which clearly come from the guest water molecules, according to the FT-IR spectra of HP-Cu-BTC. Carboxylate groups in BTC have symmetric and asymmetric stretching vibrations at 1,632/1,580 cm^{-1} and 1,447/1,374 cm^{-1}, respectively. The C-O-Cu stretching vibration absorption maxima are located around 1,116 cm^{-1} and 940 cm^{-1}, respectively. The weak and narrow bands at 2,926/2,851 cm^{-1} and 1040 cm^{-1} may be ascribed to the benzene ring's γ(C-H) and δ(C-H) vibrations. Cu-BTC has unique absorption peaks between 761 cm^{-1} and 725 cm^{-1} owing to the replacement of Cu on the benzene ring. The Cu-O stretching vibration might be responsible for the peaks at 489 cm^{-1}. The enhanced Cu-O stretching peak indicates that BTC coordinates to the Cu site either via its carboxyl oxygen atom or through its carbonyl oxygen atom.

After CO_2 cycle adsorption, all samples exhibit a CO_2 band at 2,349 cm^{-1}, suggesting the presence of physiosorbed carbon dioxide. Additionally, this band of HP-Cu-BTC(N,N) is more intense than those of HP-Cu-BTC(CTAB) and HP-Cu-BTC(SDBS) after adsorption at 303 K, which is consistent with HP-Cu-BTC(N,N) absorbing more CO_2 (SDBS). Along with the symmetrical stretching vibration of O-C=O, the 1,347 cm^{-1} peak also contains the quiet symmetric stretching modal of adsorbed CO_2. The increase in intensity might be explained by the effect of CO_2 coordination on the atmosphere of all these ligands [61]. FT-IR results are in conformity with those found in previous works about the structure of HP-Cu-BTCs adsorbents.

Fig. 2 shows the TG and DTG curves for the HP-Cu-BTCs before (upper half) and after (bottom half) CO_2 adsorption. The strength of the first stage weight loss peaks below 100 °C was reduced after CO_2 cycle adsorption, suggesting that during the degassing process, some weakly adsorbed chemicals and/or physically adsorbed water were released [62-64]. The second stage weight loss peaks between 300 °C and 360 °C represent decomposition of carboxylic groups [65]. It is clear that the HP-Cu-BTC(CTAB) ligand's environment is more influenced by the coordination of CO_2 to Cu sites following CO_2 cycle adsorption compared to HP-Cu-BTC(N,N) and HP-Cu-BTC(SDBS). This might be because N-decane was added to the cetyltrimethylammonium bromide (CTAB) template. This agrees with the FT-IR spectrum. After 450 °C, the weight loss is attributed to the full dissolution of the BTC units [66,67], which is followed by the collapse of the HP-Cu-BTCs framework. The total weight loss of HP-Cu-BTC(SDBS) and HP-Cu-BTC(N,N) before and after CO_2 adsorption is so different, which can be attributed to the electron transfer between Cu^{2+} and CO_2 at the coordination unsaturated metal site to form covalent bond interaction. The van der Waals force between the pore center and the pore window of CO_2 and HP-Cu-BTC(SDBS) and HP-Cu-BTC(N,N) adsorbates raised the weight loss temperature of HP-Cu-BTC (SDBS) and HP-Cu-BTC (N,N) after CO_2 adsorption.

2. XPS

XPS is a flexible method to determine the composition and chemical state of HP-Cu-BTCs that have been produced. The XPS spectra of HP-Cu-BTC(CTAB), HP-Cu-BTC(N,N) and HP-Cu-BTC(SDBS) were measured, Fig. 3 shows the comparable findings. the full-range XPS survey verified the existence of Cu, O, N, and C elements in all the samples [68]. As seen in Fig. 3(b), the Cu 2p XPS spectra of the HP-Cu-BTC samples are identical to

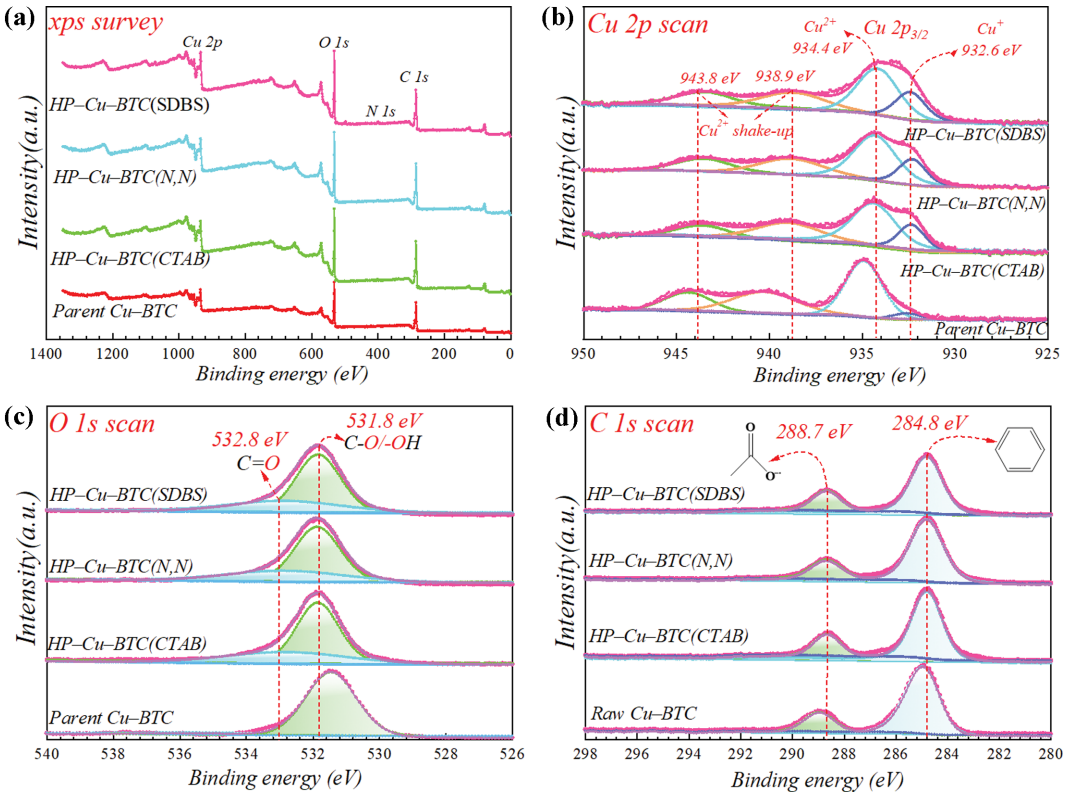


Fig. 3. XPS spectra of HP-Cu-BTC and parent Cu-BTC. (a) Survey, (b) Cu 2p, (c) O 1s, and (d) C 1s.

those of the parent Cu-BTC, with the primary peaks located about 933 eV and corresponding to the Cu $2p_{3/2}$ peaks. Fittings of the Cu $2p_{3/2}$ peaks revealed two main components with binding energies of 934.4 eV and 932.6 eV, respectively, attributed to the surface Cu^{2+} and Cu^{+} species [69], confirming the presence of CuO and Cu_2O. The presence of Cu^{2+} species in the HP-Cu-BTC samples was further verified by the shake-up satellite peaks at 943.8 eV and 938.9 eV. Due to the poor crystallinity of the Cu^{+} species, no apparent Cu_2O diffraction peak was seen in the XRD patterns. Fig. 3(c) shows the O1s spectrum, where the high-resolution spectra of O1s could be separated into two peaks at 532.8 and 531.8 eV. The peak at 532.8 eV corresponds to the oxygen components on the carboxylate groups (O-C=O) due to the residues of organic ligand or surface adsorbed oxygen species (-OH), and the peak at 531.8 eV may be ascribed to the lattice oxygen species, attributed to the formation of Cu-O-C bond in the samples. The C 1s spectrum (Fig. 3(d)) shows two obvious characteristic peaks near 284.8 eV and 288.7 eV, corresponding to the phenyl and carboxyl groups in the material [70-73], respectively. With the XPS data, we list the Cu^{+} concentration over HP-Cu-BTC in Table S3, and the Cu^{+} calculation results based on the peak areas in the XPS spectra.

3. Morphology

SEM examination was used to characterize the microstructure, morphology, and particle shape of synthesized samples; SEM micrographs are presented in Fig. 4. The findings shown in Fig. 4 reveal that the HP-Cu-BTCs have almost identical particle sizes with an octahedral morphology [74], indicating that the addition of templating agent will not interfere with the formation of crystal shape. There are, nevertheless, noticeable changes in the crystal surfaces and particle sizes; the crystal size of HP-Cu-BTC(CTAB) is distributed within the range 25-35 μm and the crystal size of HP-Cu-BTC(SDBS) is between 35 and 45 μm. While HP-Cu-BTC(N,N) shows much smaller and distorted crystals ranging from 15 to 25 μm, which would result in defects of its crystallinity. At the same time, as seen in Fig. 4(b), HP-Cu-BTC(N,N) contains structural faults and a consistent distribution of visible worm-like holes on the crystal surface. This fact implies that HP-Cu-BTC(N,N) can not only provide abundant adsorption sites but also facilitate the mass transport. In addition, compared with the conventional Cu-BTC (~10 μm), the particle size of HP-Cu-BTCs is significantly increased, the edges become smooth, and the surface is porous, which may indicate that the addition of the template agent promotes the development of the octahedral structure.

To verify whether the pore structure will be blocked as the amount of CO_2 adsorption increases, thereby changing the surface morphology of the HP-Cu-BTCs adsorbents, the study compared the microscopic morphology and porous structure changes of HP-Cu-BTCs before and after five CO_2 adsorption cycles. From Fig.

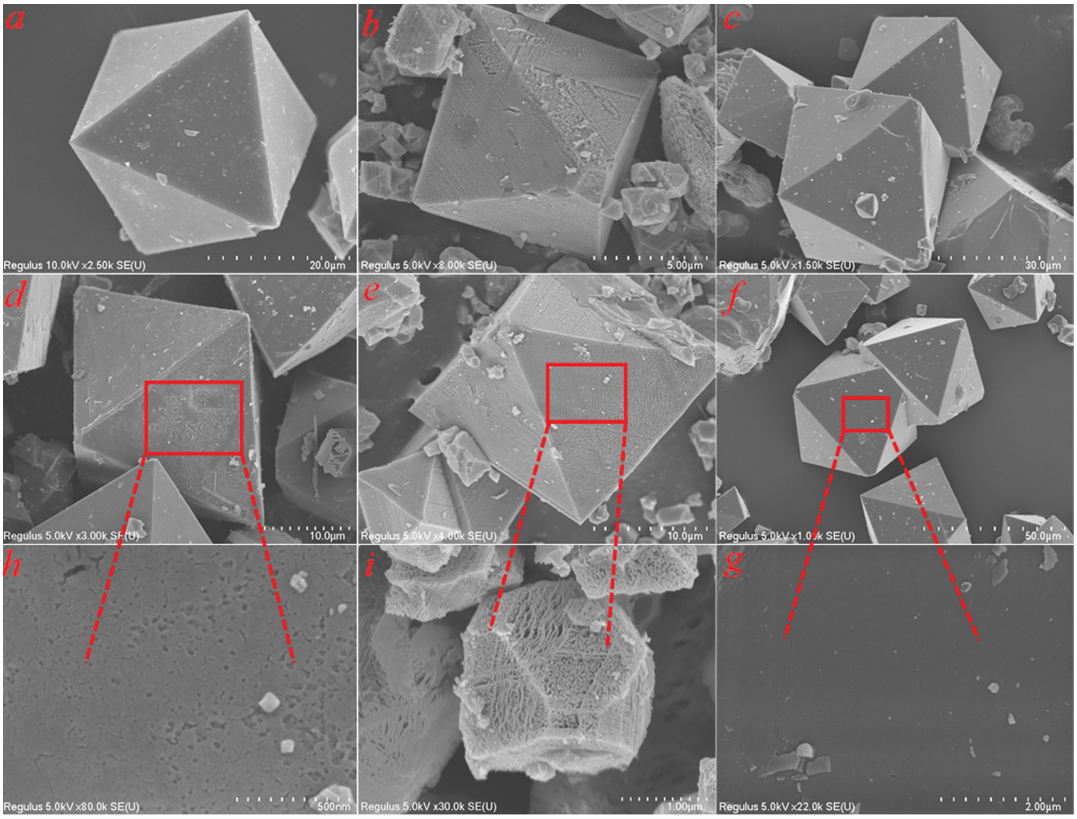


Fig. 4. FESEM images of (a)-(c) fresh HP-Cu-BTCs, (d)-(f) HP-Cu-BTCs after CO_2 adsorption cycles, (h)-(g) Enlarge HP-Cu-BTCs.

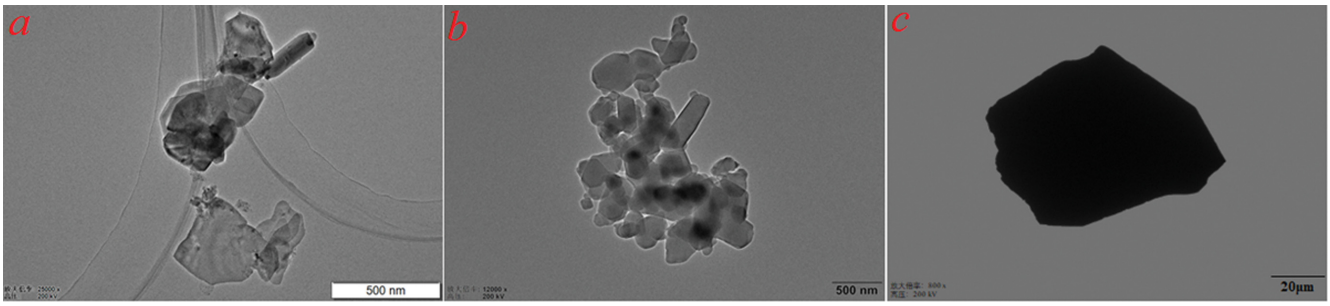


Fig. 5. TEM images of fresh adsorbents: (a) HP-Cu-BTC(CTAB), (b) HP-Cu-BTC(N,N) and (c) HP-Cu-BTC(SDBS).

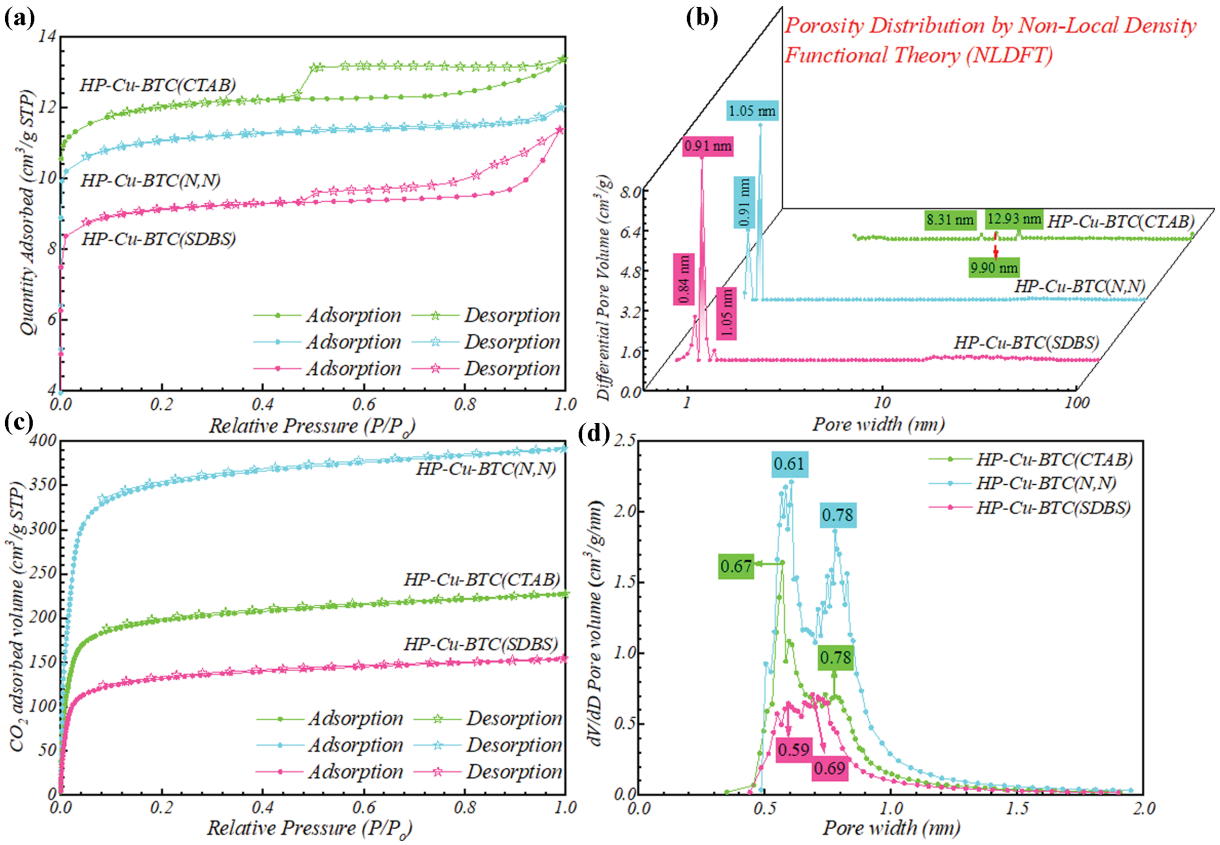


Fig. 6. (a) the N_2 adsorption (solid symbol) and desorption isotherms (open symbol) of HP-Cu-BTC, (b) differential pore-size distribution of HP-Cu-BTC for N_2 (calculated by using a slit pore NLDFT model), (c) CO_2 adsorption-desorption isotherms at 195 K of HP-Cu-BTC, and (d) Horvath-Kawazoe (H-K) ultra-microporous pore size distributions of HP-Cu-BTC for CO_2.

4(d)-(g), for all the three HP-Cu-BTCs adsorbents, their morphology and porous structure were maintained very well after five CO_2 adsorption cycles. It gives a hint that the HP-Cu-BTCs crystals were highly stable during the CO_2 adsorption/desorption experiments.

Since SEM only provides the external morphology, including the shape and size of the secondary (aggregated) particles, we further investigated the shape and size of the primary (single) crystals of the MOFs with the aid of TEM. The pictures of all HP-Cu-BTCs samples clearly show the enlarged pore structure, as shown in Fig. 5. It is worth noting that the mesopores of HP-Cu-BTC (SDBS) are mainly between the particles (Fig. 4(c) and Fig. 5(c)), which are formed by the accumulation of HP-Cu-BTC(SDBS) nanoparticles, while HP-Cu-BTC(CTAB) and HP0Cu-BTC(N,N) are mainly intra-crystalline (Fig. 4(a), (b) and Fig. 5(a), (b), respectively). Additionally, we observed that HP-Cu-BTCs exhibited considerably varied N_2 adsorption capabilities and hysteresis loop geometries (Fig. 6(a)), indicating that the porosity of HP-Cu-BTCs is template-dependent. Therefore, the porosity of HP-Cu-BTC is affected by both the amount and the type of template.

4. Specific Surface Area and Pore Size Distribution

Fig. 6(a) shows the N_2 adsorption-desorption isotherms at 77 K, whereas Fig. 6(b) shows the HP-Cu-BTC NLDFT pore-size distributions. Previous studies have shown that microporous materials with diameters of less than 0.86 nanometers (e.g., Cu-BTC) exhibit

a type I adsorption isotherm, in which microporous materials have a crystalline structure [75]. N_2 adsorption-desorption isotherms of the synthesized HP-Cu-BTC with an H1 hysteresis loop are generally type I and type IV IUPAC isotherms with the addition of the template [76]. When the relative pressure was small, the three different HP-Cu-BTC samples exhibited type I isotherms. At this time, microporous monolayer adsorption occurred, the adsorption capacity increased rapidly, and the adsorption capacity was large. When the relative pressure reached ~0.45, the adsorption and desorption isotherms of HP-Cu-BTC(CTAB) and HP-Cu-BTC(SDBS) exhibited obvious hysteresis loops (H_4-type hysteresis), respectively [77], characteristic of typical mesoporous materials, indicating that the samples synthesized with the template CTAB and SDBS had rich mesoporous structures. However, HP-Cu-BTC(N,N) only has a small hysteresis loop, indicating that the addition of the neutral organic amine formed a less mesoporous structure with an average meso pore size of only 3.12 nm. However, the specific surface area of HP-Cu-BTC(N,N) was larger than those of HP-Cu-BTC (CTAB) and HP-Cu-BTC(SDBS) because the non-ionic surfactant in the neutral organic amine did not dissociate in water and was not affected by factors like the electrolyte and solution pH. There is no strong electrostatic interaction between anions and

Table 1. The porous characteristics of HP-Cu-BTC

Adsorbent	S_{BET} ($m^2 \cdot g^{-1}$)	S_{micro} ($m^2 \cdot g^{-1}$)	S_{micro}/S_{meso}	V_{total} ($cm^3 \cdot g^{-1}$)	V_{micro} (H-K) ($cm^3 \cdot g^{-1}$)	V_{meso} ($cm^3 \cdot g^{-1}$)	Micro pore size (nm)	Primary size (μm)
CTAB	817.46	720.36	7.42	0.46	0.41	0.075	0.69	27.80
N,N	1,194.06	1,053.51	7.49	0.63	0.68	0.041	0.72	20.89
SDBS	619.94	549.99	7.86	0.39	0.26	0.086	0.68	43.33

S_{BET}: Brunauer-Emmett-Teller specific surface area. S_{micro}: micropore specific surface area are calculated using t-plot. S_{meso}: mesopore specific surface area are calculated by subtracting S_{micro} from S_{BET}. V_{total}: total pore volume calculated from the single-point adsorption branch of the N_2 isotherm at p/p_0=0.995. V_{micro}: micropore volume based on the H-K (Original) method using CO_2 adsorption branch around p/p_0=0.3. V_{meso}: mesopore volume is calculated using the BJH cumulative specific adsorption volume of holes with widths ranging from 1.7000 nm to 300.0000 nm. The micropore average pore width is determined by the H-K (Original) method of CO_2 isotherm at 195 K. The primary size (μm) is determined by SEM.

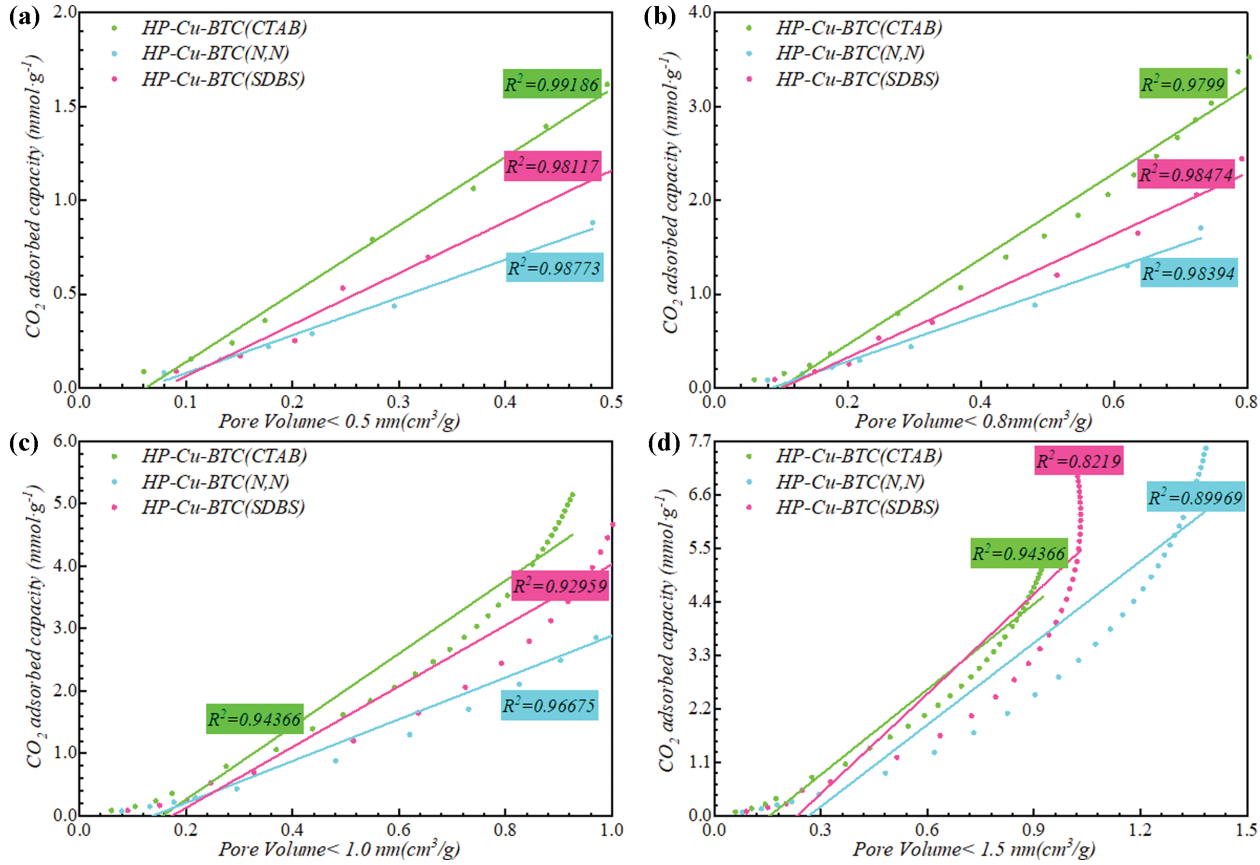


Fig. 7. Relationships of CO_2 adsorbed capacity (273 K) and the micropores volume of pores smaller than (a) 0.5 nm, (b) 0.8 nm, (c) 1.0 nm and (d) 1.5 nm.

cations formed by atoms through the gain and loss of electrons. Through hydrogen bonding and reaction precursors, materials can be formed with high specific surface areas.

Pore size engineering is a widely established technique for CO_2 collection (Fig. 6(b), (d)). A substantial volume and surface area of pores with diameters of 0.5-0.7 nm or smaller (also called ultramicropores) should be present since they have a greater capacity for CO_2 adsorption than larger supermicropores (0.7-2 nm) or mesopores (>2 nm). As a result, the adsorption was examined in relation to the differential pore volume. As seen in Fig. 7, the primary determinant of CO_2 uptake is the micropore volume of porous adsorbents. Eq. (S3) illustrates how to calculate the coefficient of determination R^2. Coefficients of determination are consistently greater for holes with a volume less than 1.0 nm. For bigger pore sizes, a greater dispersion of CO_2 adsorption data may be seen. As seen in Fig. 6(c), HP-Cu-BTC(N,N) has an abnormally high capacity for CO_2 absorption at 195 K. Because HP-Cu-BTC(N,N) has a considerable number of holes smaller than 0.8 nm, it is possible that the Ångstrïn-sized pore volume plays a significant role in the physisorption of CO_2.

As seen for Fig. 7, the adsorption isotherm of CO_2 obtained at 273 K shows that when the pore size exceeds 1.0 nm, the correlation between the adsorption capacity of CO_2 and the pore volume or surface area is insufficient. Instead, the volume of pores smaller

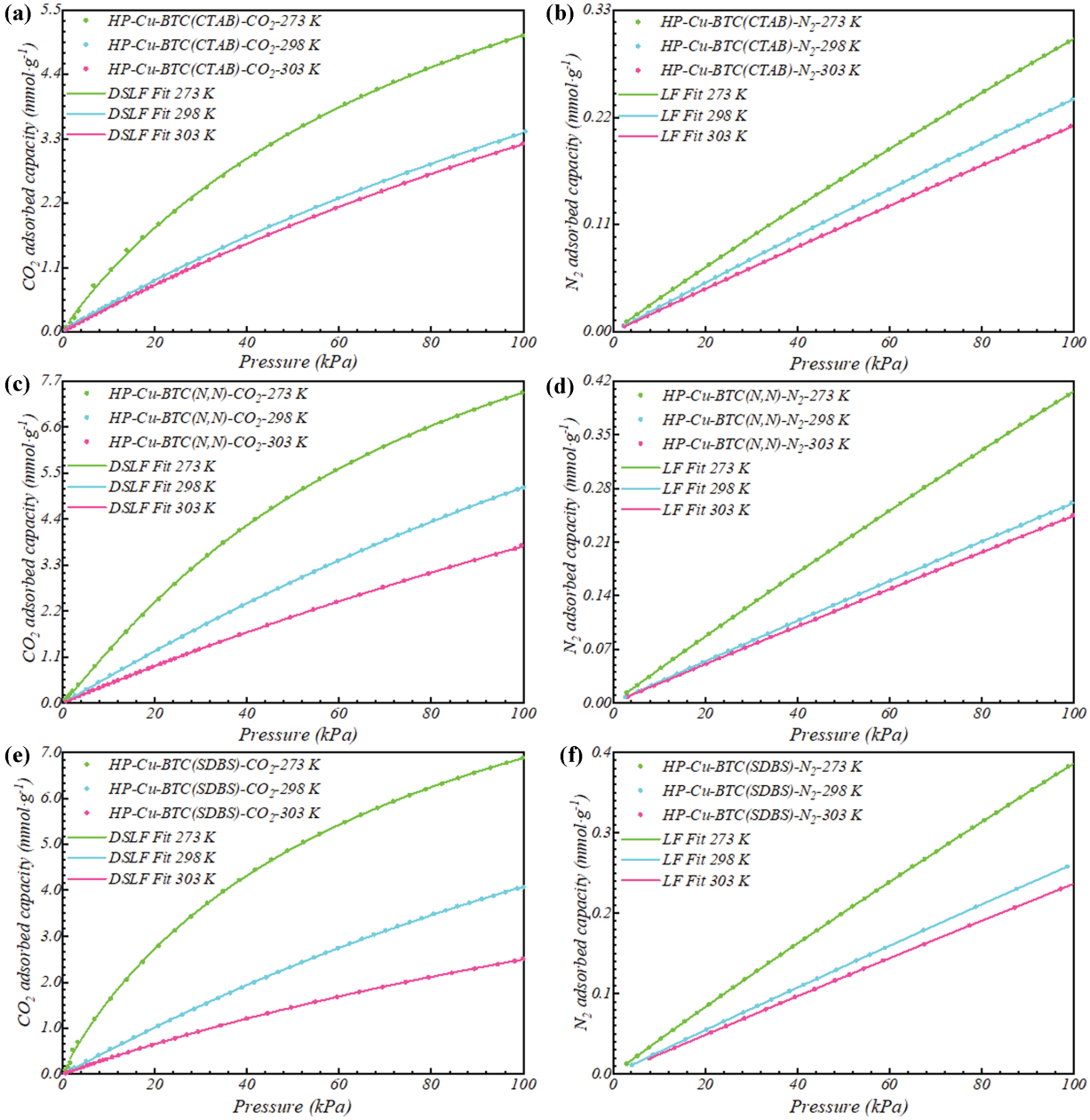


Fig. 8. Pure component CO_2 and N_2 adsorptions on (a), (b) HP-Cu-BTC(CTAB), (c), (d) HP-Cu-BTC(N,N) and (e), (f) HP-Cu-BTC(SDBS) at 273 K (green), 298 K (blue) and 303 K (pink). Solid lines correspond to fits to the CO_2 and N_2 data employing dual-site and single-site Langmuir-Freundlich models, respectively.

than 0.8 or 0.5 nm has a good linear correlation with CO_2 absorption, respectively (Fig. 7(a) and 7(b)). Thus, pores smaller than 0.8 or 0.5 nm, respectively, contribute the greatest to CO_2 absorption. Nevertheless, the volume of pores smaller than 5 Å is relatively small, which leads to a low CO_2 uptake, indicating that narrowing the pore size distribution can hardly improve the CO_2 uptake at room temperature and low pressures. Furthermore, the correlation of pores smaller than 0.5 nm is slightly better than that that of other pores. As long as the particular adsorption occurs in the pore space, this result does not lessen the significance of open copper centers.

5. CO_2 and N_2 Adsorption Isotherms on HP-Cu-BTCs

The CO_2 and N_2 adsorption isotherms on HP-Cu-BTC(CTAB), HP-Cu-BTC(N,N), and HP-Cu-BTC(SDBS) at 273, 298 and 303 K in the 0-100 kPa pressure range are shown in Fig. 8. It can be shown that neither CO_2 nor N_2 approaches saturation loading in the pressure range 0-100 kPa. At 273, 298 and 303 K, all species exhibit monolayer-type adsorption (i.e., the normal type I form of the IUPAC classification). This indicates that all isotherms are typical Langmuir types, demonstrating the HP-Cu-BTCs' microporous characteristics. The quantity of CO_2 adsorbed on all materials diminishes when the temperature rises, which might be harmful explained by a weaker gas-solid contact and the molecules' increased thermal energy at higher temperatures [78]. As can be observed, these isotherms demonstrate a rapid rise in the quantity of CO_2 adsorbed at pressures below 40 kPa, followed by a gradual increase at pressures between 40 and 100 kPa. The first rise occurred as a consequence of monolayer adsorption in micropores, while the second occurred as a result of multilayer adsorption in mesopores and adsorbate-adsorbate interactions. Additionally, the sharp increase in CO_2 absorption at low pressure is thought to be due to the unique interactions between quadrupolar CO_2 molecules and partial positively charged ions on the coordinatively unsaturated metal sites in HP-Cu-BTC in the extremely narrow pores [79]. These locations should contain the most energetic adsorption centers. As recommended by Zhou et al. [80] and Wu et al. [81]. in contrast, the absence of high-affinity binding sites in HP-Cu-BTCs results in a linear N_2 adsorption isotherm among all temperatures, similar to that reported with activated carbons [82]. In general, compared to CO_2, the isotherms of N_2 are linear, indicating that the interaction between N_2 and HP-Cu-BTC adsorbents is weaker.

The kinetic diameters of CO_2 and N_2 are known to be 3.30 and 3.64 Å, respectively [83]. CO_2 has a high interaction with the surfaces of HP-Cu-BTC adsorbents due to its substantial quadrupole moment (13.4×10^{-40} C·m^2) and polarizability (and 26.3×10^{-25} cm^3). While N_2 has a weak quadrupole moment (4.7×10^{-40} C·m^2) and lower polarizability (17.7×10^{-25} cm^3) than CO_2. This pattern may be explained by the fact that when the quadrupole moment increases, the adsorption capacity increases proportionately [84]. Furthermore, the three-dimensional microporous structure of HP-Cu-BTC and the direct interaction of CO_2 molecules with the unsaturated copper ions of the metallic cluster are credited with the high affinity of CO_2 molecules for HP-Cu-BTC [85]. To clarify this, note that the Cu atoms are coordinated to four O atoms of the tritopic linker and one H_2O molecule. The development of coordinative vacancies on the Cu active center is enabled by the dehydration of the water molecules, resulting in the formation of active unsaturated metal sites for CO_2 sorption. The larger CO_2 uptake capacity of HP-Cu-BTC(N,N) may be credited not only to the large pore volume and large specific surface area, but also to an increase in the surface dispersive forces of HP-Cu-BTC(N,N) due to the advent of the neutral organic amine (N,N-dimethyltetradecylamine (N,N)) and the specific interaction between Lewis acidic metal sites and CO_2.

Table S5 shows some of the most common CO_2 adsorbents described in the literature. At 273 K and 100 kPa, the CO_2 capture capacity of HP-Cu-BTC(N,N) (7.4293 mmol/g) is greater than that of other Cu-BTC adsorbents at 273 K and 100 kPa.

6. Dual-site Langmuir-Freundlich (DSLF) Model

It was found that the DSLF model (see Eq. (S1) and (S2) in the Supporting material) was best able to match the isotherms of CO_2 and N_2 at varying temperatures. Table S4 and Fig. 8 indicate that the model closely matches the equilibrium data. According to Table S4, the average relative error between associated findings and experimental data is given. The experimental isotherms and conclusions of the DSLF and SSLF model are in perfect accord, as seen by the ARE/% values.

7. Prediction of Adsorption Isotherm of CO_2/N_2 Mixed Gas

CO_2 is retained at a fairly modest partial pressure of 0.15 bar in post-combustion flue gas, which is discharged at a total pressure of around 1 bar. As a result, CO_2 adsorption capability in the low-pressure zone is crucial. The adsorption isotherms calculated by IAST for CO_2/N_2 (15 vol% : 85 vol%) mixtures on (a) HP-Cu-BTC(CTAB), (b) HP-Cu-BTC(N,N), and (c) HP-Cu-BTC(SDBS) as functions of total bulk pressure are shown in Fig. 9. Because CO_2 and the HP-Cu-BTCs have greater electrostatic interaction, CO_2 was preferred adsorbed over N_2 on three adsorbents. As a result, the amount of N_2 adsorbed in the mixtures was much less than that of the single-component adsorption system, owing to the high, competitive adsorption of CO_2. According to Fig. 9, the CO_2 and N_2 isotherm on HP-Cu-BTC(N,N) was greater than that on HP-Cu-BTC(CTAB) and HP-Cu-BTC(N,N) in the system with the CO_2 and N_2 mixture (SDBS). HP-Cu-BTC(N,N) had a greater CO_2/N_2 adsorption selectivity than HP-Cu-BTC(CTAB) and HP-Cu-BTC(N,N) (SDBS). The result can be confirmed from breakthrough experiments for 15% CO_2 and 85% N_2. The IAST adsorption selectivity also confirmed that CO_2 can be successfully separated from N_2.

8. CO_2/N_2 Adsorption Selectivity on HP-Cu-BTCs

Adsorptive selectivity is a significant metric for determining an adsorbent's affinity for a particular chemical. The differential in affinity of distinct gases to be attached to the surface of adsorbents is attributable to the adsorptive selectivity. In physisorption-based selectivity, physical properties of gas molecules such as quadrupole moment, polarizability, small kinetic diameter and dipole moment, all play an important role in the separation of gas mixtures. However, determining an adsorbent's adsorption selectivity for a particular gas in gas mixtures is a significant difficulty [86].

The flue gas from a post-combustion process has a very small amount of CO_2 (15%) and a significant amount of N_2 (85%). To sequester only pure CO_2 into geological formations, it is critical to extract CO_2 selectively from flue gas. The selectivity of CO_2 over N_2 in a gas mixture containing 0.15 bar CO_2 and 0.85 bar N_2 is often used to predict the performance of a material as a prospective can-

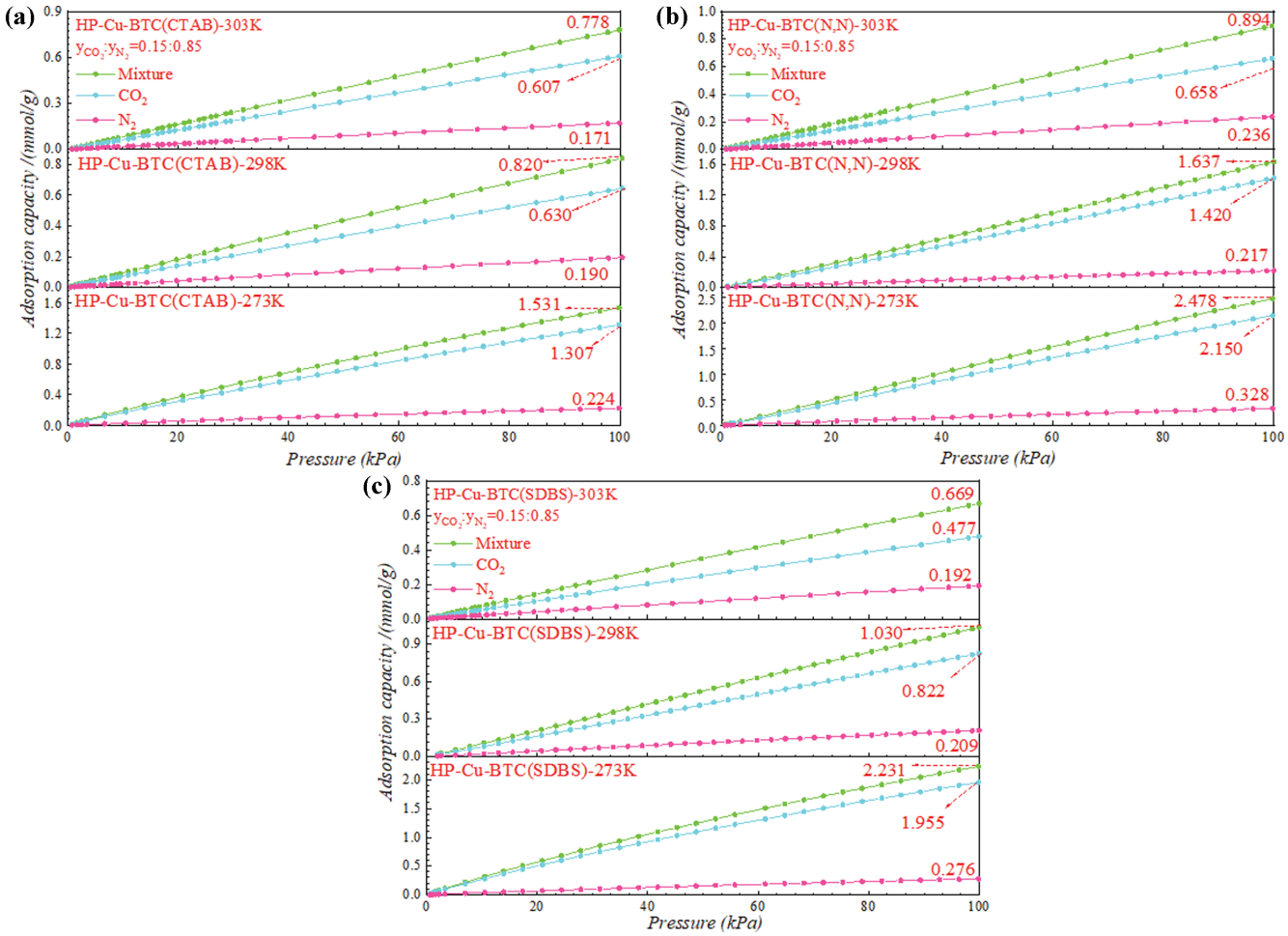


Fig. 9. IAST predicted isotherms for 15% CO_2 and 85% N_2 on the three HP-Cu-BTCs depending on the overall pressure in the system at 273, 298 and 303 K. (a) HP-Cu-BTC(CTAB), (b) HP-Cu-BTC(N,N) and (c) HP-Cu-BTC(SDBS).

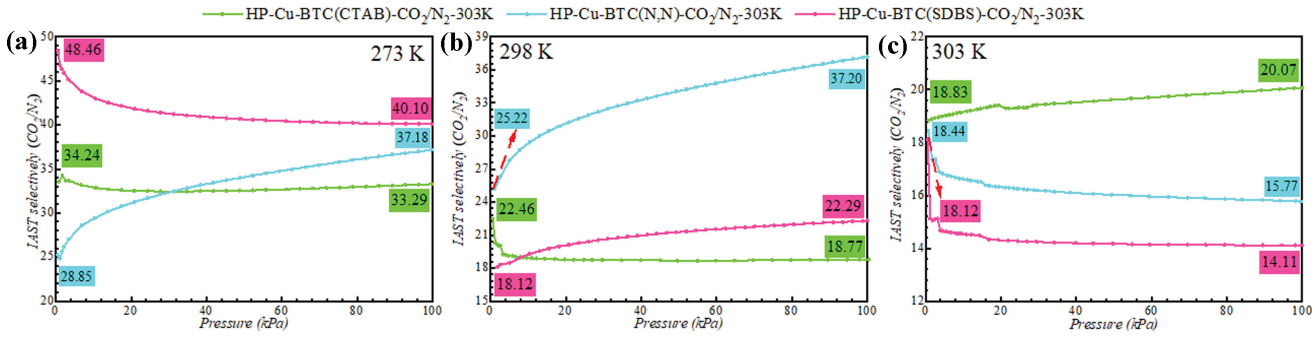


Fig. 10. IAST selectivity of HP-Cu-BTC(CTAB)-green, HP-Cu-BTC(N,N)-blue, HP-Cu-BTC(SDBS)-pink for CO_2/N_2 mixtures at (a) 273 K, (b) 298 K and (c) 303 K.

didate adsorbent for a practical application based on the composition of the flue gas. Based on the single-component isotherms of relevant gases, the CO_2 selectivity can be predicted through many methods. For example, the CO_2 selectivity can be predicted from the IAST, or the ratio of the adsorption capacity of CO_2 to the adsorption capacity of N_2 and ratio of the initial isotherm slopes.

8-1. IAST Selectivity

To calculate the selectivity of binary gas mixtures for adsorption, IAST is commonly used. At equilibrium, the chemical potential of the adsorbed solution is thought to be the same as that of the gas phase [87]. The accuracy of IAST's mixed adsorption predictions for specific materials and gas molecules has been confirmed in several research investigations as well [88,89].

The DSLF and SSLF models accurately predicted the CO_2 and N_2 isotherms at varied temperatures, respectively. The IAST was used to determine CO_2/N_2 adsorption selectivity based on DSLF model

fitting parameters (see Eq. (S12)). The CO_2/N_2 molar ratio in flue gas streams is close to 15/85 at 1 bar total pressure [37]. The CO_2/N_2 selectivity was determined at various temperatures using the IAST (see Fig. 10). Because the increase in CO_2 uptake was substantially greater than the rise in N_2 uptake, as the pressure was raised the CO_2/N_2 adsorption selectivity improved. In addition, because of CO_2's tiny kinetic diameter, the channel's adsorption sites are more numerous [90]. In general, raising the pressure reduces selectivity because CO_2 has a greater polarizability (CO_2: 29.1×10^{-25} cm^{-3}; N_2: 17.4×10^{-25} cm^{-3}), a greater quadrupole moment (CO_2: 13.4×10^{-40} $C\cdot m^2$; N_2: 4.7×10^{-40} $C\cdot m^2$), and a stronger interaction with open metal copper sites than N_2. It is expected that the selectivity will decrease as the temperature rises since the binding energy of CO_2 and N_2 is less significant as the temperature rises. Up to 37.18 selectivity for CO_2 and N_2 adsorption were found at 100 kPa for HP-Cu-BTC(N,N). Because of its high CO_2/N_2 adsorption selectivity and high CO_2/N_2 adsorption capacity, HP-Cu-BTC(N,N) has the potential to be an effective adsorbent for the separation of CO_2/N_2 mixtures.

8-2. Adsorption Selectivity Factor

Additionally, it is preferable to calculate the selectivity for CO_2/N_2 using adsorption capability of about 15 kPa for CO_2 and 85 kPa for N_2 at a combined pressure of around 1 bar. CO_2 has an adsorption capacity of 0.6085 mmol/g at 15 kPa and N_2 only has an ad-

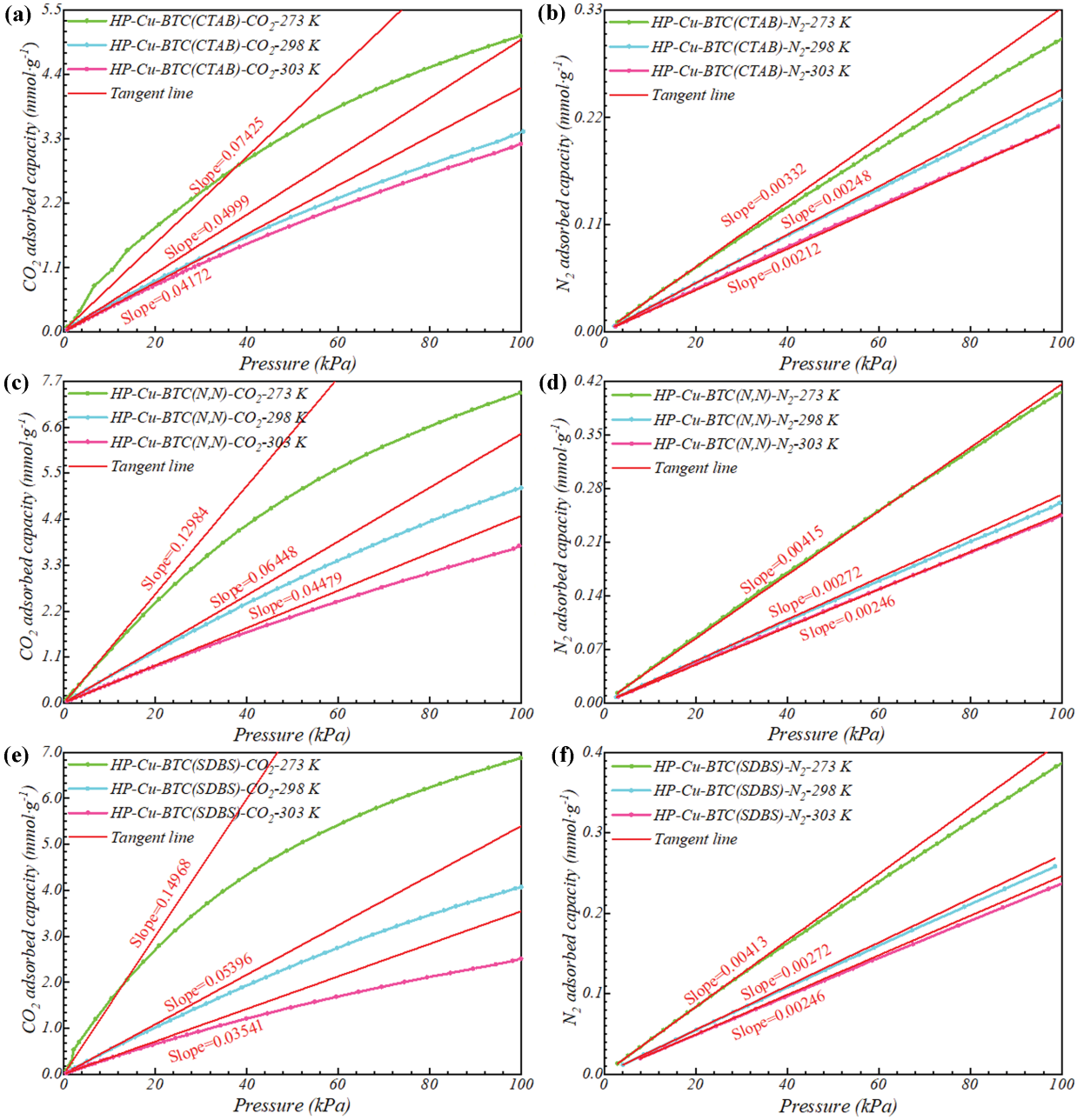


Fig. 11. CO_2 and N_2 isotherm and the tangent line of the CO_2 and N_2 isotherm in low pressure region at 273, 298 and 303 K. (a), (b) HP-Cu-BTC(CTAB), (c), (d) HP-Cu-BTC(N,N) and (e), (f) HP-Cu-BTC(SDBS).

sorption capability of 0.1809 mmol/g at 85 kPa at 303 K for HP-Cu-BTC(CTAB). As a result, the selectivity of CO_2/N_2 at 273 K is 30.834, as derived from the pure-component isotherms using Eq. (S13). Using the simplified selectivity computation is compatible with the IAST model, which is more physically precise. Although the value is lower than that of Cu-BTC [91,92], it is nonetheless comparable to some of the most promising MOFs with good CO_2/N_2 selectivity, suggesting that HP-Cu-BTCs may be an ideal choice for post-combustion CO_2 collection.

8-3. Henry's Law Selectivity

Using the IAST method, you not only need to make sure the single-component isotherms are fitted correctly based on the right models, but also has many restrictions in its application. Considering a small error (in the absolute value) for a weakly adsorbed gas can produce a very large error in the selectivity. In addition, flexible or heterogeneous adsorbents, adsorbates with significantly different adsorbing abilities (e.g., CO_2/N_2), and molecular sieves with different accessible surfaces for different adsorbates are not suitable for IAST [93]. Therefore, the predicted selectivity should be regarded as qualitative measure rather than quantitative measure. Additionally, the IAST factor does not account for the total adsorption of mixed gas molecules on the pore surface, since it is determined by single-component isotherms. However, it may be a helpful measure for evaluating a gas mixture's simple adsorptive selectivity in MOFs in order to assess suitable materials for post-combustion CO_2 collection. Thus, we measured the initial slopes of the CO_2 and N_2 adsorption isotherms and used the ratios of these slopes to calculate the CO_2 adsorption selectivity over N_2 (Fig. 11). According to these data, the computed CO_2/N_2 selectivity of HP-Cu-BTC (CTAB), HP-Cu-BTC(N,N), and HP-Cu-BTC(SDBS) was 22.364, 31.287, and 36.242 at 273 K, respectively (see Table S6), demonstrating the high CO_2/N_2 selectivity of these materials in comparison to previously reported materials.

9. HP-Cu-BTCs with Isosteric Heat of CO_2 and N_2 Adsorption

It is also critical to consider the adsorbent's regeneration energy in industrial applications. As a consequence, the virial method was utilized to compute the adsorption's isosteric heat (Q_{st}) (see Eq. (S19)). As seen in Fig. 12, all adsorbates have isosteric heats that do not remain constant as adsorption capacity increases. These significant changes are explained by better interactions between molecules in the adsorbed phase, emphasizing the energy heterogeneity of the adsorbent surface. Additionally, the isometric heat of adsorption of HP-Cu-BTCs for CO_2 is larger than that for N_2, suggesting that it has a stronger adsorption force for CO_2. This finding is in agreement with the adsorption isotherm.

The initial isosteric heat of adsorption is a critical metric for evaluating the adsorption interaction between the adsorbent and the adsorbate. These values can indicate the strongest adsorption site (such as exposed unsaturated metal sites) and the force of the adsorbents, and it is usually called isometric heat of adsorption under zero coverage condition. The isosteric heat of CO_2 adsorption for HP-Cu-BTC(CTAB), HP-Cu-BTC(N,N) and HP-Cu-BTC(SDBS) at zero surface coverage is 16.31, 22.32 and 29.82 kJ/mol, respectively. This demonstrates unequivocally that various HP-Cu-BTCs adsorbents exhibit varying degrees of affinity for CO_2 interaction at low coverage. At low coverage, the comparatively high temperatures of adsorption are due to CO_2 and open copper sites have a strong quadrupolar interaction. With an increase of CO_2 adsorbed amounts, the three HP-Cu-BTCs show a gradual increase first and then decrease of their isosteric heats of adsorption values, due to the adsorption sites' heterogeneity [94,95]. Even at high surface coverage, the isosteric CO_2 adsorption heats (Q_{st}) remain almost constant for HP-Cu-BTC(N,N); the adsorption centers of this substance have a strong affinity for CO_2 retention. This is because a huge number of micropores with widths close to 0.6 nm exist (see Fig. 6 and Table 1). Additionally, the tendency of Q_{st} remains steady as the surface coverage increases, indicating that the tiny holes and their copper cores are still not saturated by CO_2 under the circumstances of our experiment. This is an excellent characteristic for using the sample as a CO_2 collecting medium at high pressures.

To understand the isosteric heats of adsorption in the three HP-Cu-BTCs adsorbents, the interaction of adsorbed molecules with the surface of the adsorbent material must be taken into account. Utilizing a sorbent with two distinct kinds of pores (micropores and mesoporous) results in distinct adsorption methods. The mesoporous provide gas molecules with "primary adsorption sites", nev-

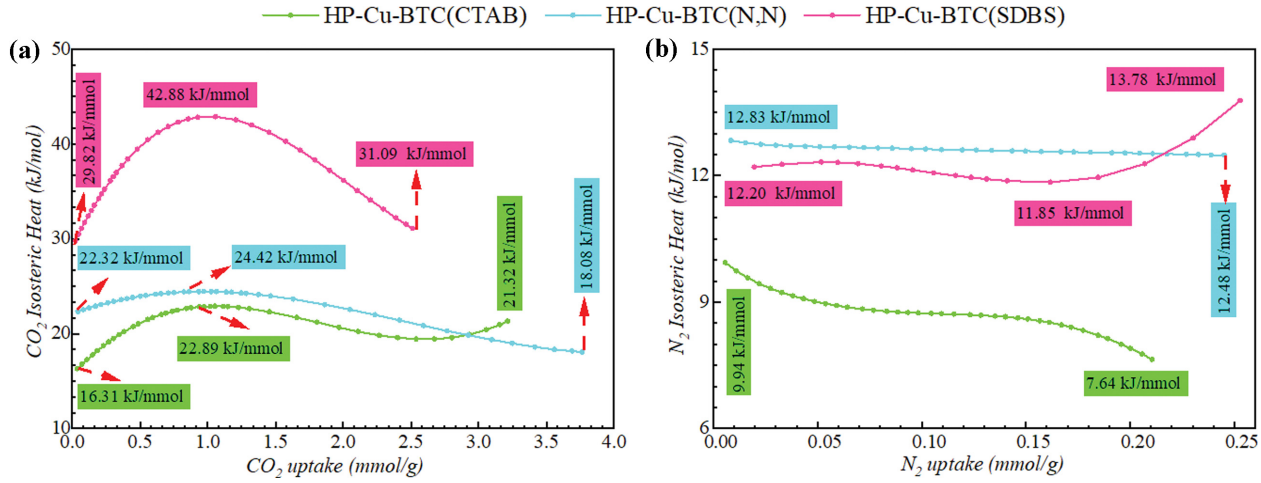


Fig. 12. The Q_{st} for CO_2 (a) and N_2 (b) on HP-Cu-BTCs calculated by virial equation.

ertheless, micropores are not capable of directly adsorbing molecules from the gas phase. Instead, initial molecules that have been adsorbed reach the open end of the pore and are re-adsorbed on "secondary sites" by diffusion processes [96]. Additionally, with increased surface covering or adsorption loading, adsorbed molecules often interact with one another (adsorbed-adsorbed interactions) [97]. According to the model described above. At zero coverage, the Q_{st} of molecules adsorbed by a diffusion process is smaller than the Q_{st} determined from main adsorption sites and adsorbed-adsorbed contact, and increases as the number of adsorbed molecules increases.

When the CO_2 adsorption capacity is around 1.0 mmol·g^{-1}, the values of Q_{st} are SDBS-(31.09 kJ·mol^{-1})>CTAB-(21.32 kJ·mol^{-1})>N,N-(18.08 kJ·mol^{-1}). The Q_{st} of CO_2 on the HP-Cu-BTC(CTAB) and HP-Cu-BTC(N,N) are lower than Cu-BTC (30 kJ·mol^{-1}) [79]. The lower values for this MOF series are potentially advantageous in terms of decreased energy consumption during adsorbent renewal. Specifically, using a material that has a high affinity for CO_2 will raise the cost of regeneration due to the significant amount of energy needed to disrupt adsorbent-CO_2 interactions.

10. Kinetics of Adsorption

Adsorption kinetics research contributes to a better knowledge of the chemical adsorption process, as well as the adsorption and reaction mechanisms. Adsorption kinetics models are often used to assess adsorption processes. Three typical adsorption kinetics models are used to evaluate the adsorption processes: a pseudo-first order model, a pseudo-second order model, and an intraparticle diffusion model. The first-order model captures the reversible interaction between the adsorbent and the adsorbate, and it is thus a more accurate representation of the CO_2 adsorption behavior of the physical adsorbent than the second-order model [98,99]. It is assumed in the second-order model that the adsorbent and the adsorbate are coupled via the formation of an extremely strong chemical bond and, as a result, the model is able to predict more accurately the CO_2 adsorption property of the chemical adsorbent [100]. Adsorption is principally controlled by intraparticle diffusion, according to the intraparticle diffusion concept. The adsorption of HP-Cu-BTCs followed pseudo-first-order kinetics because of the favorable fit between experimental and calculated values of Q_e (R^2 values above 0.999). Table S8 contains the kinetic constants and R^2, but the pseudo-second-order and intraparticle diffusion models (Fig. S7) could not adequately match the experimental results. This revealed that physical adsorption may be the rate-limiting step in the adsorption of HP-Cu-BTCs. Second, the figure created for the intraparticle-diffusion model has three subsections rather than a single straight line, demonstrating that intraparticle diffusion is not the deciding step in the rate.

The kinetics of the adsorption process were investigated, and the findings are shown in Fig. 13. As seen in Fig. 13, the adsorption capacities of the three adsorbents first grow substantially with increasing contact time during the first 20 minutes then rapidly stabilize after approximately 30 minutes. The early stage's rapid adsorption may be explained by the existence of exposed active sites on the adsorbents. As the adsorption progresses, the CO_2 molecules adsorbed on HP-Cu-BTCs gradually increase, resulting in an increase in the diffusion resistance of CO_2 molecules into the particles, so the adsorption rate becomes slower and slower. Additionally, the greatest adsorption capacity of the three adsorbents is HP-Cu-BTC(N,N), and the adsorption ability of the four ranks as HP-Cu-BTC(N,N)>HP-Cu-BTC(SDBS)>HP-Cu-BTC(CTAB).

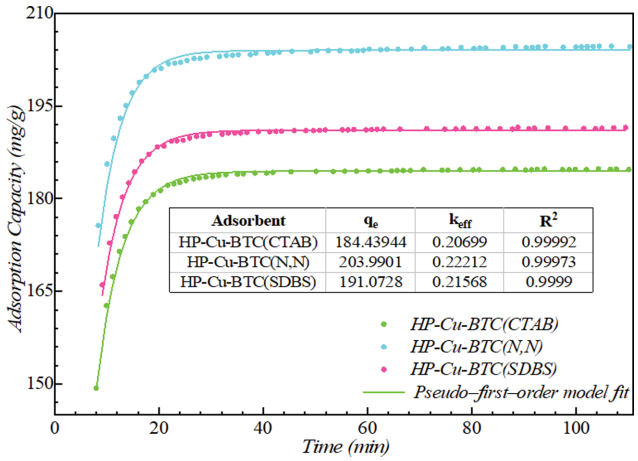


Fig. 13. Adsorption kinetics curves of CO_2 on the HP-Cu-BTC(CTAB)-green, HP-Cu-BTC(N,N)-blue and HP-Cu-BTC(SDBS)-pink at 298 K and 100 kPa (Points: experimental values, lines: fitting results, pseudo-first-order model model).

11. CO_2/N_2 Breakthrough Experiments

Considering that the adsorption and separation behaviors of many adsorbent-adsorbate systems are still difficult to predict, direct measurement of the related data is obviously very important, even if it is only for academic purposes. Compared with the case of single-component isotherms, the measurement of mixture isotherms is very complicated and time-consuming. Among the various measurement methods, fixed-bed breakthrough is the most widely adopted, because it closely resembles the industrial separation operations. Using breakthrough setups, the adsorption and separation performance under a given temperature, pressure, and mixture composition (including water and other interfering components) can be readily controlled. The breakthrough times of the adsorbates directly reveal their relative adsorption tendencies, which are combinations of the thermodynamic and kinetic effects. When the outlet flow rate of each adsorbate is measured, the adsorbate uptake at any time can be obtained by integrating the breakthrough curve. However, measurement of the outlet flow rate is much more difficult than that of the relative concentration.

To further validate the practicality of the method for industrial use, capability for CO_2 adsorption was computed using breakthrough curves generated in a fixed-bed reactor with simulated flue gas (CO_2: 15%, N_2: 85%) at 298 K and 1 atm. As shown in Fig. 14, efficient separation for CO_2/N_2 mixtures has been factually achieved. For the breakthrough of CO_2/N_2 mixture, N_2 had a very fast elution through the packed bed at 147.27 s, 185.41 s and 168.46 s, whereas CO_2 did not begin to flow out until 301.96 s, 679.14 s and 509.62 s for HP-Cu-BTC(CTAB), HP-Cu-BTC(N,N) and HP-Cu-BTC(SDBS), respectively. CO_2 was retained in the column for a remarkable period prior to saturating the HP-Cu-BTCs. For HP-Cu-BTC(SDBS), the N_2 breakthrough curve has a little roll-up in the ordinate direction (the intensity of the output gas ions sur-

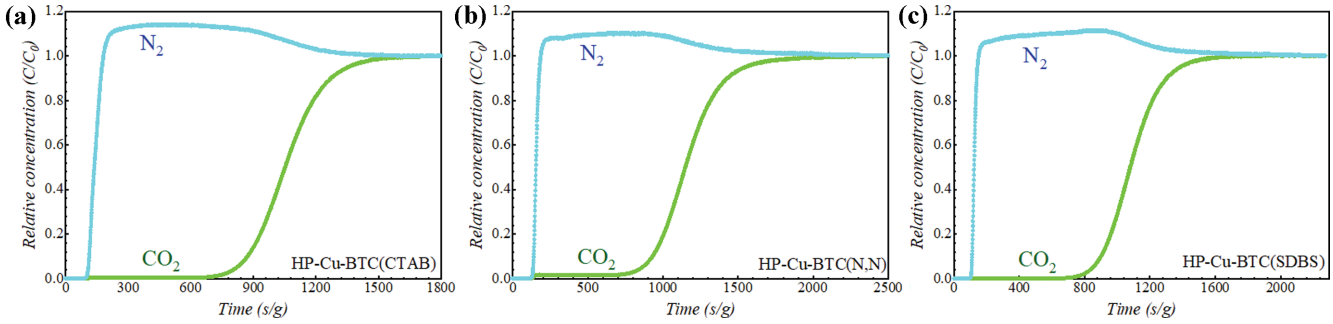


Fig. 14. Column breakthrough experiment for a CO_2/N_2 (15 : 85, v : v) gas mixture (298 K, 1 atm) carried out on (a) HP-Cu-BTC(CTAB), (b) HP-Cu-BTC(N,N) and (c) HP-Cu-BTC(SDBS).

passes the intensity of the input gas ions). When the concentration front of CO_2 progresses in the column, the roll-up may be ascribed to the desorption of N_2 induced by CO_2.

Because actual mixed-gas separation occurs under kinetic flow conditions, which are often non-equilibrium, the selectivity anticipated by IAST may differ greatly from the selectivity seen in actual mixed-gas separation [101,102]. From breakthrough curves, the separation selectivity based on the saturation adsorption capacity was 7.6296, 7.4831 and 8.8014, respectively. Because the CO_2/N_2 selectivity values that were found are smaller than the values that were found from IAST, these values may be more accurate for real selectivity. This means that HP-Cu-BTCs have real dynamic selectivity of CO_2 over N_2. It can be used in real-world post-combustion CO_2 capture. Moreover, a volumetric adsorption device is unable to assess regenerability/cycle stability; however, mixed gas breakthrough makes this information available.

Table S9 shows the CO_2 saturation adsorption capabilities. The CO_2 saturated adsorption capacity of HP-Cu-BTC(CTAB) and HP-Cu-BTC(SDBS) was 13.289 and 13.665 $cm^3 \cdot g^{-1}$ at 298 K and 1 atm, respectively. While the HP-Cu-BTC(N,N) showed better CO_2 saturated adsorption capacity (14.534 $cm^3 \cdot g^{-1}$) than that of HP-Cu-BTC(CTAB) and HP-Cu-BTC(SDBS). It was previously assumed that the CO_2 adsorption capability of HP-Cu-BTCs mainly depends on unsaturated Cu-metal sites. For the HP-Cu-BTC(SDBS), the improved CO_2 adsorption capability of was ascribed to the Cu^+ percentage (18.17/%). While for the HP-Cu-BTC(N,N), the CO_2 adsorption capacity had higher CO_2 adsorption capacity (7.429 $mmol \cdot g^{-1}$) in spite of low Cu^+ percentage (15.67%). As a result, it was fair to assume that the CO_2 adsorption capacity of HP-Cu-BTC(N,N) was determined not only by the unsaturated Cu-metal sites, but also the proportion of microporous volume and specific surface area. According to Table S9, N_2 shows higher diffusion coefficients than CO_2 on the three HP-Cu-BTCs. This strongly suggests that adsorption rate of N_2 is faster than CO_2. Indeed, the homogeneous microporous found on the surface of HP-Cu-BTCs, as shown in SEM and TEM pictures, may have a critical role in regulating such diffusion processes.

12. CO_2-TPD Curve on HP-Cu-BTCs

CO_2-TPD is mostly used to define adsorption sites on adsorbents and to calculate the strength of the adsorbate-adsorbent interaction [103]. The CO_2-TPD curve for HP-Cu-BTCs within the range of temperatures 100-400 °C is shown in Fig. 15 for reference. At

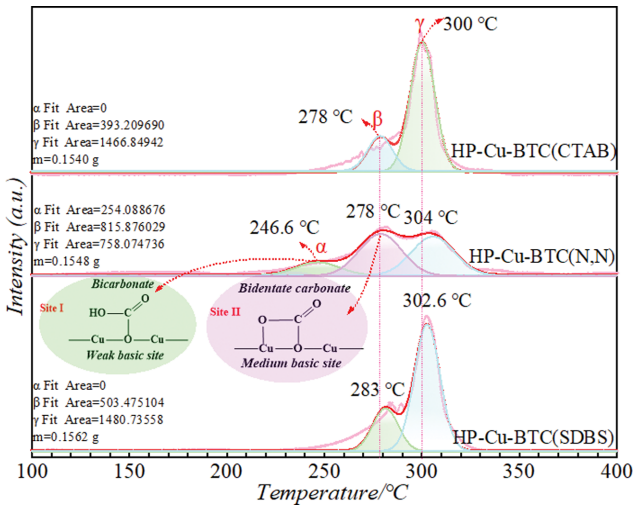


Fig. 15. CO_2-TPD profiles of HP-Cu-BTC(CTAB), HP-Cu-BTC(N,N) and HP-Cu-BTC(SDBS).

246.6 °C, the first peak (peak) is related to bicarbonate, which was formed when CO_2 molecules were slightly adsorbed at basic OH groups in the HP-Cu-BTC(N,N) system. It also can be seen from the peak area that this site is a weak basic site with weak intensity. For the three samples, the second CO_2 desorption peak appears near 280 °C; it may be attributable to the desorption of CO_2 from unsaturated Cu-metal sites, which implies that the open metal sites made electrostatic contact with the CO_2 quadrupole moments [81]. The order of its adsorption capacity is HP-Cu-BTC(N,N)>HP-Cu-BTC(SDBS)>HP-Cu-BTC(CTAB) according to the corresponding peak area underneath the CO_2-TPD curve. Besides the slight shift of the peaks to lower temperatures, and the peak intensity of HP-Cu-BTC(N,N) is higher than that of HP-Cu-BTC(SDBS). The findings further confirmed that the relationship between CO_2 and the open metal sites of HP-Cu-BTC(N,N) was greater than that between CO_2 and HP-Cu-BTC(CTAB) and HP-Cu-BTC(SDBS), but that the electrostatic interaction was less than the chemical bond, enabling CO_2 molecules to be desorbed easily. The third peak (peak) was ascribed to organic ligand degradation, which was consistent with the TG data (Fig. 2).

HP-Cu-BTC is shown in Fig. 16. It looks like this: There are two kinds of huge central cavities (L_2 and L_3), which are both 9 Å in

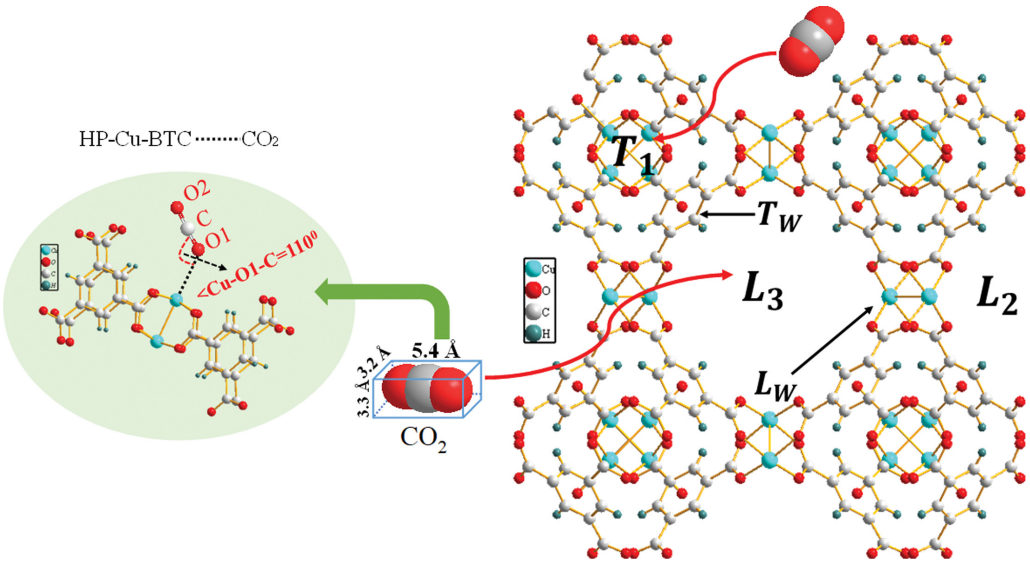


Fig. 16. Possible CO_2 adsorption mechanism on the HP-Cu-BTCs adsorbents.

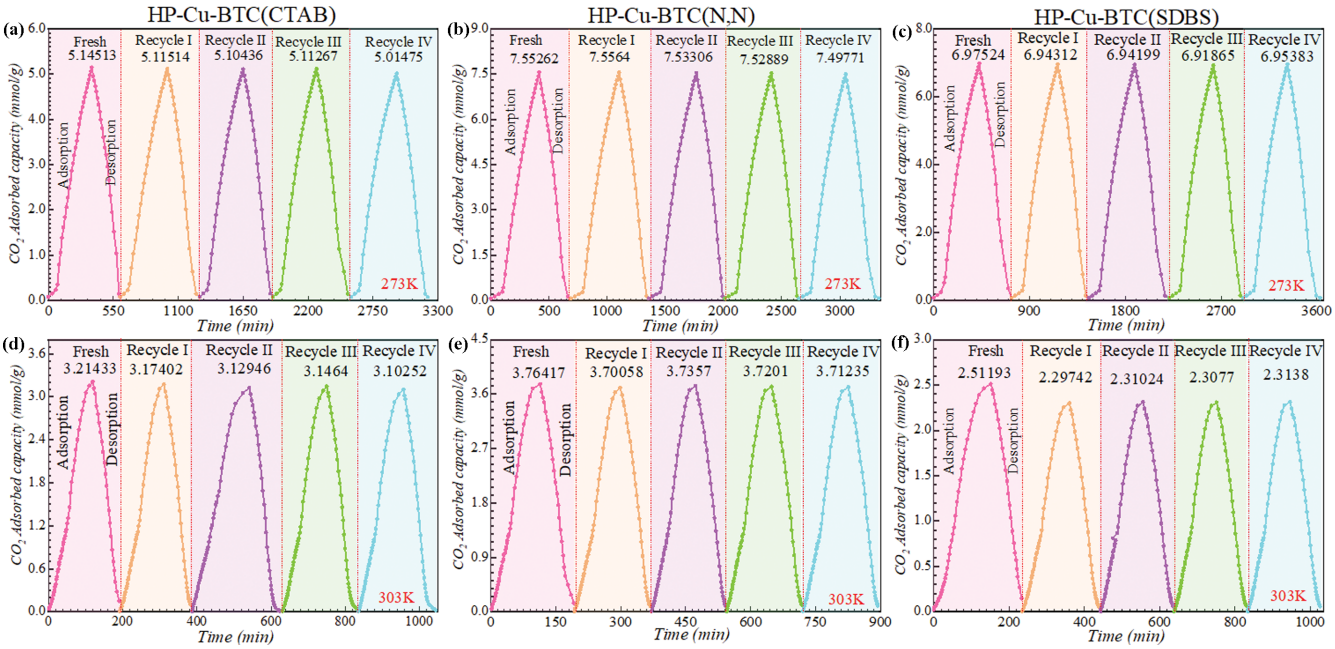


Fig. 17. Five CO_2 adsorption/desorption isotherm cycles on (a), (d) HP-Cu-BTC(CTAB), (b), (e) HP-Cu-BTC(N,N) and (c), (f) HP-Cu-BTC (SDBS) at 273 and 303 K.

diameter, surround small cavities (T_1), which are both 5 Å in diameter. As a result, we also set up two more places. These are the triangular-shaped apertures connecting T_1 and L_3 (T_w), as well as the windows connecting the two huge chambers L_2 and L_3 (T_w) [104]. Both experiments and molecular simulations have shown that these sites can be reached [105-107]. It has the same size and form as L_2, but only L_3 contains open copper sites that point into the pore. These van der Waals interactions, which are important at high coverages, and specific interactions with the copper atoms, which might offer more binding sites to the molecules that are adsorbing them at low coverages, are both possible [108-110].

According to the CO_2-TPD data, the HP-Cu-BTCs may have two major adsorption sites. The tiny pore cage T_1 (site I) is one, whereas the open Cu site L_3 is another (site II) [111]. As seen in Fig. 16, T_1's triangular windows absorb CO_2 molecules through the van der Waals force, which is readily desorbed. It is believed that the electrostatic force is responsible for CO_2 adsorption on open Cu sites (L_3).

13. Regenerability of HP-Cu-BTCs in Multiple Cycles

The reusability of the adsorbent is critical in practical applications. Five successive cycles of CO_2 adsorption-desorption on HP-Cu-BTCs were carried out to ascertain the regenerability and operating capacity of the material. Fig. 17 illustrates the reversibility of the CO_2 adsorption process on HP-Cu-BTCs at 273 and 303 K. As seen

in Fig. 17, there is a tiny degree of hysteresis between the adsorption and desorption curves, and the quantity of CO_2 adsorbed in the low-pressure region drops somewhat after the first cycle. This might be because the strong interaction between HP-Cu-BTCs and CO_2 resulted in the inadequate desorption of the adsorbed CO_2 molecules at 273 and 303 K [112,113]. Adsorption and desorption cycles are repeated five times in a row; the total CO_2 capture capacity of the HP-Cu-BTC(CTAB), HP-Cu-BTC(N,N), and HP-Cu-BTC(SDBS) is approximately 97.5%, 99.3%, and 99.7% of the maximum adsorption capacity, respectively, at 273 K and 96.5%, 98.6%, and 92.1%, respectively, at 303 K. This finding implies that the CO_2 capacity loss after five adsorption-desorption cycles is negligible. More importantly, the powder XRD pattern (Fig. 1(a)) and FT-IR spectra (Fig. 1(b)) of the HP-Cu-BTCs adsorbents after being used five times were determined to be similar to that of the fresh adsorbent.

CONCLUSIONS

HP-Cu-BTC(CTAB), HP-Cu-BTC(N,N), and HP-Cu-BTC(SDBS) exhibit ultra-high CO_2 adsorption capacity (5.0699, 7.4293, and 6.8783 mmol/g) at 273 K and 100 kPa, respectively, which is greater than many outstanding adsorbents discussed in the literature [114]. The XRD, FT-IR, TG, and adsorption kinetics analyses all corroborated the physical capture of CO_2 on all of the examined adsorbents. We also showed that for HP-Cu-BTCs with high CO_2 binding sites, a DSLF adsorption model is required. Metal-organic frameworks with promise are not limited to those that have open metal sites. The particular surface, pore size, and pore volume all play a role. HP-Cu-BTC(N,N) exhibits the greatest performance in terms of adsorption capacity and regenerability because of its large specific surface area (1,194.06 m^2/g) and total pore volume (0.63 cm^3/g). As a result, the three samples' CO_2 adsorption process is mostly governed by physisorption as assessed by S_{BET}. Despite the fact that pore size and volume are insufficient predictors of CO_2 absorption by HP-Cu-BTCs adsorbents, the pore volume of micropores has a substantial correlation with the quantity of CO_2 adsorbed. At ambient pressure, CO_2 absorption is inversely proportional to the volume of pores having a pore diameter of less than or equal to 1.5 nm. The strongest association between CO_2 adsorption capacity and pore volume occurs when the pore size is smaller than 0.5 nm. This relationship may be utilized to improve the design of CO_2 adsorbents and carbon capture and storage (CCS) systems.

According to isotherms for pure-component substances, the binary-mixture isotherms and CO_2/N_2 adsorption selectivity of the samples were estimated using IAST. The binary mixture's anticipated isotherms indicated that CO_2 was more readily adsorbed than N_2. Thus, HP-Cu-BTC(N,N) adsorption selectivity for CO_2/N_2 was much larger than that of Cu-BTC. HP-Cu-BTC(N,N) adsorption selectivity for CO_2/N_2 reached up to 37.20 at 100 kPa, over 6.9 times that of Cu-BTC.

Since the quadrupole CO_2 molecules interact with unsaturated metal sites in HP-Cu-BTCs, the CO_2 isometric heat of adsorption is larger than N_2. HP-Cu-BTC(N,N) has a lower Q_{st} of CO_2 adsorption than HP-Cu-BTC(SDBS) at zero-surface coverage, implying a greater surface for CO_2 trapping in high-energy centers. The low adsorption heat saves energy on adsorbent renewal. The adsorbents retain their remarkable adsorption properties after five successive adsorption/desorption cycles. Additionally, the regeneration process is straightforward and rapid. The excellent CO_2 adsorption capability and CO_2/N_2 selectivity, and regenerability of the modified hierarchical porous Cu-BTC imply that it may be a potential cost-effective adsorbent for CO_2 capture from flue gas.

ACKNOWLEDGEMENTS

We gratefully acknowledge the financial support from the National Natural Science Foundation of China (No. 21961160741, 21938001, U1663220, 21476101), Guangdong Natural Science Foundation (No. 2022A1515011712), Maoming science and technology plan project (No. 2020515, No. 2021011).

CONFLICT OF INTEREST

There are no conflicts to declare.

LIST OF ABBREVIATIONS

BTC : benzene-1,3,5-tricarboxylate
IAST : ideal adsorbed solution theory
PSA : pressure swing adsorption
SMB : simulated moving bed
MOF : metal organic framework
GCMC : grand canonical Monte Carlo
CCS : carbon capture and storage
CTAB : cetyltrimethylammonium bromide
N,N : N,N-dimethyltetradecylamine
SDBS : sodium dodecylbenzene
XRD : X-ray diffraction
FTIR : Fourier-transform infrared
XPS : X-ray photoelectron spectroscopy
SEM : scanning electron microscopy
TEM : transmission electron microscopy
TG : thermogravimetry
DTG : differential thermal gravity
CO_2-TPD : CO_2-temperature programmed desorption
DSLF : Dual-site Langmuir-Freundlich
SSLF : Langmuir-Freundlich
NLDFT : Non-Local Density-Functional-Theory
H-K : Horvath-Kawazoe
BET : Brunauer-Emmett-Teller
CCDC : cambridge crystallographic data centre

SUPPORTING INFORMATION

Additional information as noted in the text. This information is available via the Internet at http://www.springer.com/chemistry/journal/11814.

REFERENCES

1. N. L. Rosi, J. Kim, M. Eddaoudi, B. Chen, M. O'Keeffe and O. M.

Yaghi, *J. Am. Chem. Soc*., **127**, 1504 (2005).
2. M. Feng, P. Zhang, H. C. Zhou and V. K. Sharma, *Chemosphere*, **209**, 783 (2018).
3. D. Shindell and C. J. Smith, *Nature*, **573**, 408 (2019).
4. C. Pelletier, Y. Rogaume, L. Dieckhoff, G. Bardeau, M.-N. Pons and A. Dufour, *Appl. Energy*, **235**, 1381 (2019).
5. S. E. Tanzer and A. Ramírez, *Energy Environ. Sci*., **12**, 1210 (2019).
6. P. Xia, M. Antonietti, B. Zhu, T. Heil and J. Yu, *Adv. Funct. Mater*., **29**, 1900093 (2019).
7. N. N. Vu, S. Kaliaguine and T.-O. Do, *Adv. Funct. Mater*., **29** 1901825 (2019).
8. G. Yilmaz and S. Keskin, *J. Membr. Sci*., **454**, 407 (2014).
9. H. Yang, Z. Xu, M. Fan, R. Gupta, R. B. Slimane, A. E. Bland and I. Wright, *J. Environ. Sci*., **20**, 14 (2008).
10. Y. Tan, W. Nookuea, H. Li, E. Thorin and J. Yan, *Energy Convers. Manage*., **118**, 204 (2016).
11. D. J. Barker, *BMJ*, **301**, 1111 (1990).
12. S. Chen, M. Zhu, Y. Tang, Y. Fu, W. Li and B. Xiao, *J. Mater. Chem. A*., **6**, 19570 (2018).
13. W. Wang, M. Zhou and D. Yuan, *J. Mater. Chem. A*., **5**, 1334 (2016).
14. W. Tian, H. Zhang, H. Sun, A. Suvorova, M. Saunders, M. Tade and S. Wang, *Adv. Funct. Mater*., **26**, 8651 (2016).
15. V. Benoit, N. Chanut, R. S. Pillai, M. Benzaqui, I. Beurroies, S. Devautour-Vinot, C. Serre, N. Steunou, G. Maurin and P. L. Llewellyn, *J. Mater. Chem. A*., **6**, 2081 (2018).
16. H. Thakkar, S. Lawson and A. A. Rownaghi, *Chem. Eng. J*., **348**, 109 (2018).
17. K. Lee, J. D. Howe, L. C. Lin and B. Smit, *Chem. Mater*., **27**, 668 (2015).
18. L. Zhu, X. Q. Liu, H. L. Jiang and L. B. Sun, *Chem. Rev*., **117**, 8129 (2017).
19. Q. G. Zhai, X. Bu, C. Mao, X. Zhao, L. Daemen, Y. Cheng, A. J. Ramirez-Cuesta and P. Feng, *Nat. Commun*., **7**, 1 (2016).
20. F. Zheng, D. N. Tran, B. J. Busche and G. E. Fryxell, *Ind. Eng. Chem. Res*., **44**, 3099 (2005).
21. F. Su, C. Lu, S. C. Kuo and W. Zeng, *Energy Fuels*, **24**, 1441 (2010).
22. M. B. Yue, Y. Chun, Y. Cao, X. Dong and J. H. Zhu, *Adv. Funct. Mater*., **16**, 1717 (2010).
23. T. R. C. Van Assche, T. Duerinck, J. J. G. Sevillano, S. Calero, G. V. Baron and J. F. M. Denayer, *J. Phys. Chem. C*., **117**, 18100 (2013).
24. J. B. DeCoste, G. W. Peterson, B. J. Schindler, K. L. Killops, M. A. Browe and J. J. Mahle, *J. Mater. Chem. A*., **1**, 11922 (2013).
25. Z. Zhao, X. Ma, Z. Li and Y. S. Lin, *J. Membr. Sci*., **382**, 82 (2011).
26. A. Zukal and M. Kubů, *Adsorption*, **21**, 99 (2015).
27. R. A. Sarmiento-Perez, L. M. Rodriguez-Albelo, A. Gomez, M. Autie-Perez, D. W. Lewis and A. R. Ruiz-Salvador, *Micropor. Mesopor. Mater*., **163**, 186 (2012).
28. L. Alaerts, E. Séguin, H. Poelman, F. Thibault-Starzyk, P. A. Jacobs and D. E. De Vos, *Chem. Eur. J*., **12**, 7353 (2006).
29. S. Keskin, J. Liu, J. K. Johnson and D. S. Sholl, *Micropor. Mesopor. Mater*., **125**, 101 (2009).
30. S. S. Y. Chui, S. M. F. Lo, J. P. H. Charmant, A. G. Orpen and I. D. Willians, *Science*, **283**, 1148 (1999).
31. L. Yang, H. Naruke and T. Yamase, *Inorg. Chem. Commun*., **6**, 1020 (2003).
32. D. M. D'Alessandro, B. Smit and J. R. Long, *Angew. Chem. Int. Ed*., **49**, 6058 (2010).
33. J. Gao, X. Qian, R. B. Lin, R. Krishna, H. Wu, W. Zhou and B. Chen, *Angew. Chem. Int. Ed*., **59**, 4396 (2020).
34. C. Duan, J. Huo, F. Li, M. Yang and H. Xi, *J. Mater. Sci*., **53**, 16276 (2018).
35. Y. Mao, D. Chen, P. Hu, Y. Guo and Y. Ying, *Chem. Eur. J*., **21**, 15127 (2015).
36. H. Huang, J. R. Li, K. Wang, T. Han, M. Tong, L. Li, Y. Xie, Q. Yang, D. Liu and C. Zhong, *Nat. Commun*., **6**, 8847 (2015).
37. C. Duan, H. Zhang, M. Yang, F. Li, Y. Yu, J. Xiao and H. Xi, *Nanoscale Adv*., **1**, 1062 (2019).
38. M. Du, C. P. Li, C. S. Liu and S. M. Fang, *Coord. Chem. Rev*., **257**, 1282 (2013).
39. Y. Kim, T. Yang, G. Yun, M. B. Ghasemian, J. Koo, E. Lee, S. J. Cho and K. Kim, *Angew. Chem. Int. Ed*., **127**, 13471 (2015).
40. B. Liu, Y. Li, S. C. Oh, Y. Fang and H. Xi, *RSC Adv*., **6**, 61006 (2016).
41. L. B. Sun, J. R. Li, J. Park and H. C. Zhou, *J. Am. Chem. Soc*., **134**, 126 (2012).
42. D. Bradshaw, S. El-Hankari and L. Lupica-Spagnolo, *Chem. Soc. Rev*., **43**, 5431 (2014).
43. H. Y. Guan, R. J. LeBlanc, S. Y. Xie and Y. Yue, *Coord. Chem. Rev*., **369**, 76 (2018).
44. J. Huo, M. Brightwell, S. El Hankari, A. Garai and D. Bradshaw, *J. Mater. Chem. A*., **1**, 15220 (2013).
45. M. Petkovic, K. R. Seddon, L. P. N. Rebelo and C. S. Pereira, *Chem. Soc. Rev*., **40**, 1383 (2011).
46. Z. Fang, B. Bueken, D. E. De Vos and R. A. Fischer, *Angew. Chem. Int. Ed*., **54**, 7234 (2015).
47. G. Cai and H. L. Jiang, *Angew. Chem. Int. Ed*., **56**, 563 (2017).
48. Z. Q. Li, J. C. Yang, K. W. Sui and N. Yin, *Mater. Lett*., **160**, 412 (2015).
49. H. Huang, J. R. Li, K. Wang, T. Han, M. Tong, L. Li, Y. Xie, Q. Yang, D. Liu and C, Zhong, *Nat. Commun*., **6**, 1 (2015).
50. X. Gu, Z. H. Lu and Q. Xu, *Chem. Commun*., **46**, 7400 (2010).
51. J. Li, Y. Liu, X. Wang, G. Zhao, Y. Ai, B. Han, T. Wen, T. Hayat, A. Alsaedi and X. Wang, *Chem. Eng. J*., **330**, 1012 (2017).
52. B. Li, X. Zhu, K. Hu, Y. Li, J. Feng, J. Shi and J. Gu, *J. Hazard. Mater*., **302**, 57 (2016).
53. L. Feng, S. Yuan, L. L. Zhang, K. Tan, J. L. Li, A. Kirchon, L. M. Liu, P. Zhang, Y. Han, Y. J. Chabal and H. C Zhou, *J. Am. Chem. Soc*., **140**, 2363 (2018).
54. S. C. Junggeburth, K. Schwinghammer, K. S. Virdi, C. Scheu and B. V. Lotsch, *Chem. Eur. J*. **18**, 2143 (2012).
55. C. Duan, F. Li, H. Zhang, J. Li, X. Wang and H. Xi, *RSC Adv*., **7**, 52245 (2017).
56. Y. Q. Lan, H. L. Jiang, S. L. Li and Q. Xu, *Adv. Mater*., **23**, 5015 (2011).
57. Y. Zhao, J. Zhang, B. Han, J. Song, J. Li and Q. Wang, *Angew. Chem. Int. Ed*., **50**, 636 (2011).
58. K. M. Choi, H. J. Jeon, J. K. Kang and O. M. Yaghi, *J. Am. Chem. Soc*., **133**, 11920 (2011).
59. Y. Zhao, M. Seredych, J. Jagiello, Q. Zhong and T. J. Bandosza, *Chem. Eng. J*., **239**, 399 (2014).
60. C. Petit, B. Levasseur, B. Mendoza and T. J. Bandosz, *Micropor. Mesopor. Mater*., **154**, 107 (2012).
61. Y. Zhao, M. Seredych, Q. Zhong and T. J. Bandosz, *RSC Adv*., **3**, 9932 (2013).
62. F. Zhang, J. Shi, Y. Jin, Y. Fu, Y. Zhong and W. Zhu, *Chem. Eng. J*.,

259, 183 (2015).
63. E. V. Perez, K. J. Balkus Jr., J. P. Ferraris and I. H. Musselman, *J. Membr. Sci.*, **328**, 165 (2009).
64. L. Qin, L. N. Wang, P. J. Ma and G. H. Cui, *J. Mol. Struct.*, **1059**, 202 (2014).
65. D. Hack, A. B. Dürr, K. Deckers, P. Chauhan, N. Seling, L. Rübenach, L. Mertens, G. Raabe, F. Schoenebeck and D. Enders, *Angew. Chem. Int. Ed.*, **128**, 1829 (2016).
66. B. Levasseur, C. Petit and T. J. Bandosz, *ACS Appl. Mater. Interfaces*, **2**, 3606 (2010).
67. C. Petit, B. Levasseur, B. Mendoza and T. J. Bandosz, *Micropor. Mesopor. Mater.*, **154**, 107 (2012).
68. R. S. Kumar, S. S. Kumar and M. A. Kulandainathan, *Micropor. Mesopor. Mater.*, **168**, 57 (2013).
69. K. Chen, J. L. Ling and C. D. Wu, *Angew. Chem. Int. Ed.*, **132**, 1941 (2020).
70. B. J. Zhu, X. Y. Yu, Y. Jia, F. M. Peng, B. Sun, M. Y. Zhang, T. Luo, J. H. Liu and X. J Huang, *J. Phys. Chem. C.*, **116**, 8601 (2012).
71. B. J. Zhu, X. Y. Yu, Y. Jia, F. M. Peng, B. Sun, M. Y. Zhang, T. Luo, J. H. Liu and X. J. Huang, *Chem. Eng. J.*, **334**, 1270 (2018).
72. Y. Li, J. Qi, J. Li, J. Shen, Y. Liu, X. Sun, J. Shen, W. Han and L. Wang, *ACS Sustain. Chem. Eng.*, **5**, 6635 (2017).
73. J. Shen, Y. Li, C. Wang, R. Luo, J. Li, X. Sun, J. Shen, W. Han and L. Wang, *Electrochim. Acta*, **273**, 34 (2018).
74. A. Azizi, E. A. Feijani, Z. Ghorbani and A. Tavasoli, *Int. J. Hydrogen Energy*, **46**, 2244 (2021).
75. V. F. D. Martins, A. M. Ribeiro, A. Ferreira, U. H. Lee, Y. K. Hwang, J. S. Chang, J. M. Loureiro and A. E. Rodrigues, *Sep. Purif. Technol.*, **149**, 445 (2015).
76. M. Thommes, K. Kaneko, A. V. Neimark, J. P. Olivier, F. Rodriguez-Reinoso, J. Rouquerol and K. S. W. Sing, *Pure Appl. Chem.*, **87**, 25 (2016).
77. M. C. Orilall, N. M. Abrams, J. Lee, F. J. DiSalvo and U, Wiesner, *J. Am. Chem. Soc.*, **130**, 8882 (2008).
78. M. Younas, M. Sohail, L. K. Leong, M. J. K. Bashir and S. Sumathi, *Int. J. Environ. Sci.*, **13**, 1839 (2016).
79. Z. Liang, M. Marshall and A. L. Chaffee, *Energy Fuels*, **23**, 2785 (2009).
80. C. Zhou, L. Cao, S. Wei, Q. Zhang and L. Chen, *Comput. Theor. Chem.*, **976**, 153 (2011).
81. H. Wu, J. M. Simmons, G. Srinivas, W. Zhou and T. Yildirim, *Phys. Chem. Lett.*, **1**, 1946 (2010).
82. J. A. Mason, K. Sumida, Z. R. Herm and R. Krishna, *Energy Environ. Sci.*, **4**, 3030 (2011).
83. M. Oschatz and M. Antonietti, *Energy Environ. Sci.*, **11**, 57 (2018).
84. J. J. Gutiérrez-Sevillano, J. M. Vicent-Luna, D. Dubbeldam and S. Calero, *J. Phys. Chem. C.*, **117**, 11357 (2013).
85. R. V. Siriwardane, M. S. Shen, E. P. Fisher and J. Losch, *Energy Fuels*, **19**, 1153 (2005).
86. K. Sumida, D. L. Rogow, J. A. Mason, T. M. McDonald, E. D. Bloch, Z. R. Herm, T. H. Bae and J. R. Long, *Chem. Rev.*, **112**, 724 (2012).
87. J. Y. Lee, D. H. Olson, L. Pan and T. J. Emge, *Adv. Funct. Mater.*, **17**, 1255 (2007).
88. P. Song, Y. Li, B. He, J. Yang, J. Zheng and X. Li, *Micropor. Mesopor. Mater.*, **142**, 208 (2011).
89. A. J. Hernández-Maldonado, J. Guerrero-Medina and V. C. Arce-González, *J. Mater. Chem. A.*, **1**, 2343 (2013).
90. A. Kronast, S. Eckstein, P. T. Altenbuchner, K. Hindelang, S. I. Vagin and B. Rieger, *Chem. Eur. J.*, **22**, 12800 (2016).
91. Y. Zhao, M. Seredych, Q. Zhong and T. J. Bandosz, *RSC Adv.*, **3**, 9932 (2013).
92. Y. Zhao, M. Seredych, Q. Zhong and T. J. Bandosz, *ACS Appl. Mater. Interfaces*, **5**, 4951 (2013).
93. K. Sumida, D. L. Rogow, J. A. Mason and T. M. McDonald, *Chem. Rev.*, **112**, 724 (2012).
94. B. Mu, P. M. Schoenecker and K. S. Walton, *Phys. Chem. C.*, **114**, 6464 (2010).
95. J. R. Karra and K. S. Walton, *J. Phys. Chem. C.*, **114**, 15735 (2010).
96. W. A. Steele, *The interaction of gases with solid surfaces*, Pergamon, New York (1974).
97. A. W. Adamson and A. P. Gast, *Physical chemistry of surfaces*, Interscience, New York (1967).
98. S. Loganathan, M. Tikmani, S. Edubilli, A. Mishra and A. Kumar-Ghoshal, *Chem. Eng. J.*, **256**, 1 (2014).
99. R. Serna-Guerrero and A. Sayari, *Chem. Eng. J.*, **161**, 182 (2010).
100. J. M. Borah, J. Sarma and S. Mahiuddin, *Colloids Surf. A Physicochem. Eng. Asp.*, **387**, 50 (2011).
101. Y. Zhao, K. X. Yao, B. Teng, T. Zhang and Y. Han, *Energy Environ. Sci.*, **6**, 3684 (2013).
102. P. Nugent, Y. Belmabkhout, S. D. Burd, A. J. Cairns, R. Luebke, K. Forrest, T. Pham, S. Ma, B. Space, L. Wojtas, M. Eddaoudi and M. J. Zaworotko, *Nature*, **495**, 80 (2013).
103. J. Kim, S. N. Kim, H. G. Jang, G. Seo and W. S. Ahn, *Appl. Catal. A-Gen.*, **453**, 175 (2013).
104. S. Calero, J. J. Gutiérrez-Sevillano and E. García-Pérez, *Micropor. Mesopor. Mater.*, **165**, 79 (2013).
105. C. Chmelik, J. Kärger, M. Wiebcke, J. Caro, J. M. van Baten and R. Krishna, *Micropor. Mesopor. Mater.*, **117**, 22 (2009).
106. E. García-Pérez, J. Gascón, V. Morales-Flórez, J. M. Castillo, F. Kapteijn and S. Calero, *Langmuir*, **25**, 1725 (2009).
107. C. Xue, Q. Yang and C. Zhong, *Mol. Simul.*, **35**, 1249 (2009).
108. P. D. C. Dietzel, Y. Morita, R. Blom and H. Fjellvåg, *Angew. Chem. Int. Ed.*, **44**, 6354 (2005).
109. L. J. Murray, M. Dincă and J. R. Long, *J. Mater. Chem. A.*, **17**, 3154 (2007).
110. A. Martín-Calvo, F. D. Lahoz-Martín and S. Calero, *J. Phys. Chem. C.*, **116**, 6655 (2012).
111. G. Song, X. Zhu, R. Chen, Q. Liao, Y. D. Ding and L. Chen, *RSC Adv.*, **6**, 19069 (2016).
112. Z. Hu, Y. Wang, S. Farooq and D. Zhao, *AIChE J.*, **63**, 4103 (2017).
113. Y. Chen, J. Xiao, D. Lv, T. Huang, F. Xu, X. Sun, H. Xi, Q. Xia and Z. Li, *Chem. Eng. Sci.*, **158**, 539 (2017).
114. C. Xin, H. Zhan, X. Huang, H. Li, N. Zhao, F. Xiao, W. Wei and Y. Sun, *RSC Adv.*, **5**, 27901 (2015).

Supporting Information

Enhanced CO_2/N_2 separation performance in HP-Cu-BTCs by modifying the open-metal sites and porosity using added templates

Ping Yang*, Rujin Zhou*, Youhua Zhang*, Shui Cao*, Dan Zhang*, Hongbing Ji, Linhai Duan*,†, and Xiuhong Meng*,†**

*Key Laboratory of Inferior Crude Oil Processing of Guangdong Provincial Higher Education Institutes, Guangdong University of Petrochemical Technology, Maoming 525000, P. R China
**The Key Laboratory of Low-Carbon Chemistry & Energy Conservation of Guangdong Province, Sun Yat-Sen University, Guangzhou 510275, P. R. China
(*Received 6 May 2022 • Revised 23 June 2022 • Accepted 4 July 2022*)

EXPERIMENTAL

Materials

Copper(II) nitrate hydrate ($Cu(NO_3)_2{\cdot}H_2O$, 99.99%), 1,3,5-benzenetricarboxylic acid ($C_6H_3(CO_2H)_3$, H_3BTC, 98%), N-decane ($C_{10}H_{22}$, >99.0%), the cationic surfactant cetyltrimethylammonium bromide (CTAB, $C_{19}H_{42}BrN$, 99%), the neutral organic amine N,N-Dimethyltetradecylamine (N,N, $C_{16}H_{35}N$, >90.0%) and the anionic surfactant sodium dodecylbenzene sulfonate (SDBS, $C_{18}H_{22}NaO_3S$, AR) were all purchased from Aladdin Industrial Corporation. Absolute ethanol (EtOH, AR) was purchased from XiLong Science Co., Ltd. (China) and deionized water was prepared on-site in the laboratory. All chemical reagents were used as-is and are specified in Fig. S1.

HP-Cu-BTC Hierarchical Porous Synthesis

The synthesis of HP-Cu-BTC samples were according to the previously mentioned technique by Duan et al. [1] with a few tweaks, it is mainly that the order of adding copper nitrate solution and template is different. The specific methods are shown in Fig. S2. Firstly, 2.473 g cetyltrimethylammonium bromide CTAB and 0.9655 g n-decane or 3.0303 g N,N-Dimethyltetradecylamine (N,N), this mass was the reagent divided by the purity 90%, or 2.759 g sodium dodecylbenzene sulfonate (SDBS) was added in the 100 mL beaker. Next, 5.465 g of $Cu(NO_3)_2{\cdot}3H_2O$ was added in 75 mL of water that has been deionized to produce solution A, 2.6429 g of 1,3,5-benzenetricarboxylic acid (H_3BTC) was added in 75 mL ethanol in order to produce solution B. After stirring both solutions for 0.5 hours, solution A was added drop by drop to solution B using a burette, the mixture was then agitated for 0.5 hours. Following that, the mixture was added to the templates mentioned before to produce solution C, respectively, ultrasonic stirring for 0.5 h. The final solution C was transferred into 100 mL Teflon-lined stain fewer steel autoclaves and solvothermal heated at 393 K for 12 hours. A vacuum drying oven at 423 K for 12 h removed the template and solvents trapped in the channels after cooling to room temperature. The products are designated HP-Cu-BTC(CTAB), HP-Cu-BTC(N,N), and HP-Cu-BTC(SDBS). The synthesis process for the HP-Cu-BTCs is presented in Table S1 and Fig. S2.

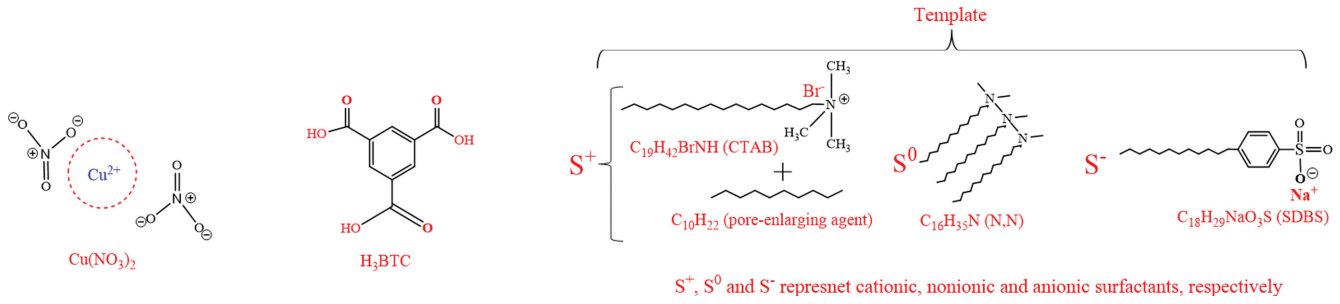


Fig. S1. The structures of precursor materials and templates used to build HP-Cu-BTCs in this work.

Table S1. Synthetic materials and ratio of HP-Cu-BTCs

Adsorbent	Templating agent	Molar ratio of (templating agent/Cu^{2+}/H_3BTC/Decane)
HP-Cu-BTC(CTAB)	CTAB	0.3 : 1.0 : 0.556 : 0.3
HP-Cu-BTC(N,N)	N,N	0.5 : 1.0 : 0.556 : 0
HP-Cu-BTC(SDBS)	SDBS	0.35 : 1.0 : 0.556 : 0

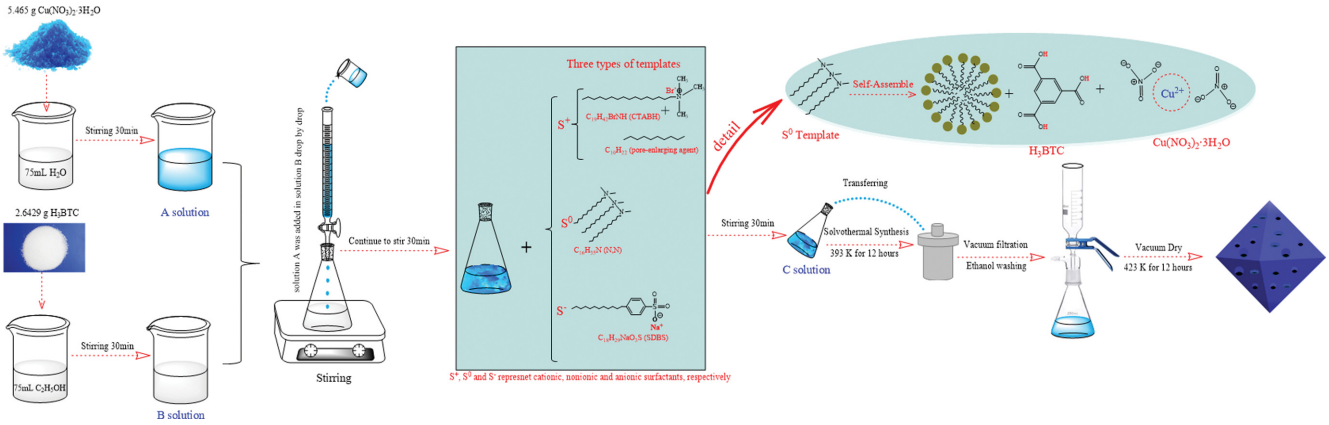


Fig. S2. Synthesis of hierarchical porous HP-Cu-BTCs.

Characterization

FESEM pictures were acquired using a Hitachi Regulus8220 at a modest loading energy (5.0 kV). The three fresh adsorbents were examined first, followed by five adsorption/desorption cycles on the sample. SEM analysis was then used to determine the structure of HP-Cu-BTCs after CO_2 adsorption. TEM investigation was completed using a Hitachi HT-7700 electron microscope set to 200 kV. At room temperature and static air conditions, Patterns of XRD were obtained using a Rigaku D/max-2000 diffractometer using Cu Ka radiation (λ=0.15418 nm, tube voltage: 40 kV, tube current: 40 mA), scanning from 5° to 50° of the diffraction angles (2θ) at a scan rate of 5°/min and a step size of 0.02°. Prior to measurements, samples were pre-treated for 12 hours at 150 °C in a vacuum oven to eliminate any remaining moisture. Diamond 4.6 software was used to mimic the XRD patterns of the MOFs utilized in this study, and the crystal structure information was acquired from the CCDC-112954 for Cu-BTC. HP-Cu-BTC porous structure was investigated using N_2 adsorption-desorption (77 K) and CO_2 adsorption-desorption (195 K, for ultra-micropores with a diameter of 1 nm) measurements on a Micromeritics ASAP 2020 HD88 specific surface area and porosity analyzer and a BeiShiDe 3H-2000PS2, respectively. Prior to the adsorption tests, the materials were outgassed under vacuum for 1 hour at 90 °C and then heated to 150 °C for 12 hours. The specific surface area was measured using the multiple-point BET technique across the relative pressure range $0.05<p/p_0<0.3$ and the micropore specific surface area was determined using the t-plot method and N_2 adsorption data. The NLDFT model and N_2 adsorption data were used to estimate pore size distributions. Pore size distributions for micropores were obtained using the H-K technique and CO_2 adsorption data. The total pore volume (V_{total}) of the samples was determined using the single-point adsorption branch of the N_2 adsorption isotherm at p/p_0=0.995, and the micropore volume (V_{micro}) was determined using the H-K (Original) technique with the CO_2 adsorption branch near p/p_0=0.3. A NETZSCH STA 449 F3 synchronous thermal analyzer was used to conduct TG studies. Approximately 20 mg of sample was heated at a rate of 5 °C/min to 900 °C under a N_2 flow rate of 30 mL/min, and weight loss was recorded continuously. The absorbance spectra were acquired using FT-IR on a Nicolet 6700 spectrometer. Prior to measurements, the samples were pre-treated for 12 hours at 150 °C in a vacuum oven. The combination was then coarsely mixed with KBr in an agate mortar to create a 1/100 mass ratio of HP-Cu-BTC-KBr. During the measurement, the resolution was set at 4 cm^{-1}. Thermo Scientific ESCALAB 250Xi spectrometer (Thermo Fisher Scientific, USA) was used to perform XPS studies using Al K (1,486.6 eV) radiation as the X-ray source (14 kV, 250 W). The XPS spectra of the materials were adjusted using carbon as a reference (C 1s, 284.8 eV).

CO_2 and N_2 Adsorption Measurements

CO_2 and N_2 isotherms adsorption tests at various temperatures (273, 298, and 303 K) were performed using an ASAP 2020 HD88 Surface Area and Porosity Analyzer to study the adsorption isotherm features of HP-Cu-BTCs samples (Micromeritics Instrument Corp., America). Temperatures were kept very stable by using a Dewar with a circulating jacket and a thermostatic bath with a 0.01 K accuracy. Before each measurement, 200-300 mg of the material was vacuumed and degassed for 1 hour at 363 K before being heated to 423 K for 8 hours. At pressures ranging from 0 to 100 kPa, adsorption isotherms were measured. Throughout the measures, ultrahigh purity He (99.999%), CO_2 (99.99%), and N_2 (99.99%) were utilized.

CO_2 Adsorption Kinetic Curves on HP-Cu-BTCs

The CO_2 adsorption kinetics were determined using the BSD-VVS&DVS Weight Method Vacuum Steam Adsorption at 298 K and 100 kPa. Prior to beginning the adsorption experiment, the three HP-Cu-BTCs adsorbents were degassed at 423 K for 12 hours in a vacuum atmosphere. Then, the adsorption kinetic curves were measured to determine the quantity of CO_2 adsorbed on the HP-Cu-BTCs as a function of time. Second, the MFC was used to regulate a CO_2 input rate of 60 mL/min to the chamber of samples. Finally, Adsorption kinetics experiment ended when the sample's weight was stable, suggesting that equilibrium had been achieved (the sample was saturated with CO_2).

CO_2 Dynamic Breakthrough Experiments

The CO_2 adsorption performance of HP-Cu-BTCs from a simulated flue gas was also examined in a fixed-bed flow adsorption system using a BSD-MAB multi-component adsorption breakthrough curve analyzer (BeiShiDe Instrument Corp., China) device for separation equipped with a fixed-bed absorber at 298 K and 1 atm, as shown in Fig. S4. In this study, 1.5-2.0 g of adsorbent (40-

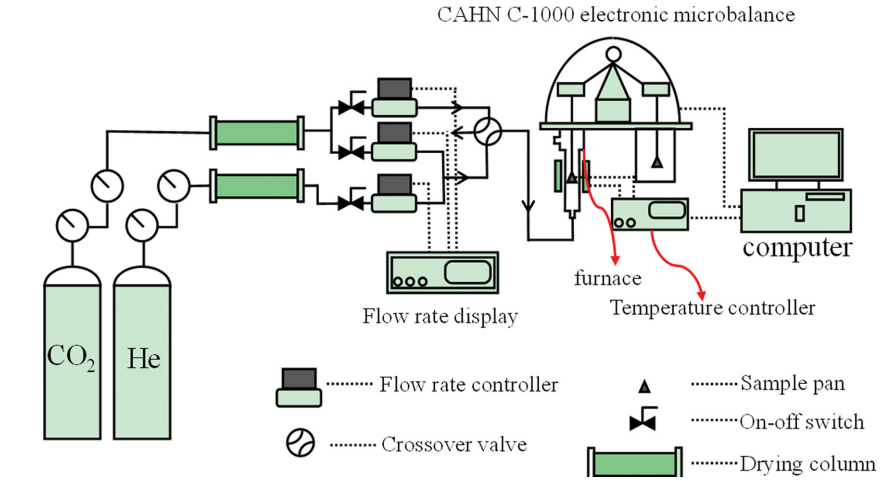


Fig. S3. Representation of the BSD-VVS&DVS gravimetric-densiometric apparatus.

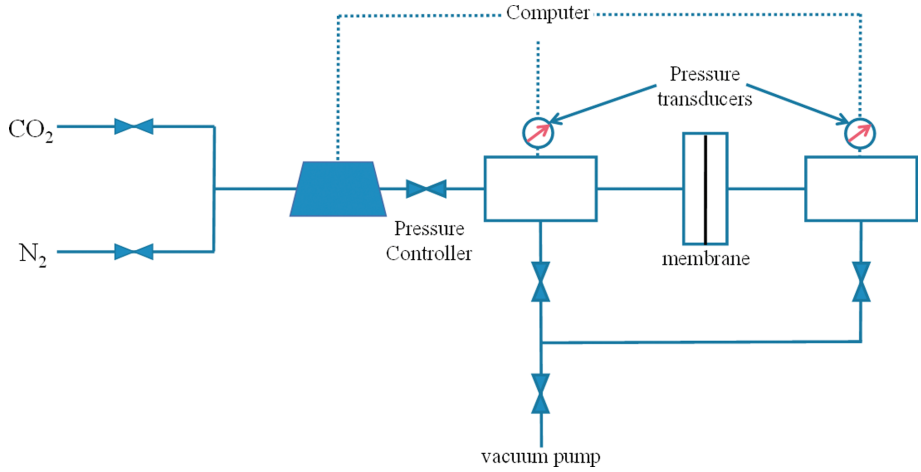


Fig. S4. Diagram of the experimental setup for measuring adsorption equilibrium.

60 mesh powder) was packed into a stainless-steel column of 75-85 cm in length and 6 mm in diameter, and the length of the packaged sample was 80 mm, and the column was then packed with quartz wool stuffed into both of its ends. Following that, the column was attached to a six-way valve through a gas chromatography analyser. Prior to the breakthrough test, the adsorbents were activated at 423 K for 2 hours in a helium atmosphere with a flow of 20 mL·min^{-1} to eliminate any moisture or pre-adsorbed CO_2 from the sample, then cooled to the adsorption temperature of 298 K in a helium environment with a flow of 20 mL·min^{-1}. The simulated flue gas (CO_2: 15%, N_2: 85%) was introduced into the adsorption column at a rate of 5 mL·min^{-1} under the supervision of a mass flow controller. The effluent composition at the column output was examined using a BSD-MASS spectrometer (INFICON America) equipped with a thermal conductivity detector (TCD). The breakthrough curves may be used to calculate the adsorption capacity.

Carbon Dioxide Temperature Programmed Desorption (CO_2-TPD)

The CO_2 temperature-programmed desorption (CO_2-TPD) technique is performed using the DAC-1000 (Ruiguwei Technology Co., Ltd., China) equipment. The following is the precise procedure: To begin, the HP-Cu-BTCs powders were compressed into a disk with a pressure of less than 5 MPa for 10 minutes, then pulverized and sieved to get 40-60 mesh particles. Then, 150 mg (40-60 mesh) of HP-Cu-BTC sample is placed in a U-shaped glass tube to prevent it from being blown away by the gas. The tube is plugged at both ends with a small amount of quartz cotton and pretreated with helium flow of 50 mL·min^{-1} at 150 °C for 1 h to ensure the sample is free of impurities. After cooling to 50 °C using helium flow, high-purity CO_2 was delivered into the sample for 2 hours, followed by 1.5 hours of flushing with helium flow of 50 mL·min^{-1} at 50 °C to remove any excess CO_2 on the sample surface. Finally, the temperature was increased to 500 °C in a He atmosphere at a rate of 10 °C/min using a 50 mL·min^{-1} helium flow. As the temperature increases gradually, the CO_2 molecules adsorbed in the sample begin to desorb, and the desorbed CO_2 gas is detected and analyzed at the quartz tube's exit by the thermal conductivity detector, and recorded on the computer to produce a curve called the CO_2-TPD curve.

Regeneration Experiments

The CO_2 adsorption/desorption recyclability of the HP-Cu-BTCs samples was also determined five times consecutively using the

Table S2. Assignments of the FT-IR bands detected after CO_2 cycle adsorption on HP-Cu-BTCs

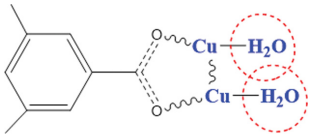
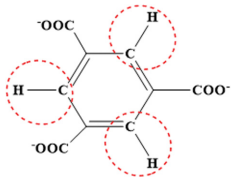
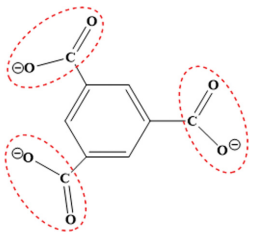
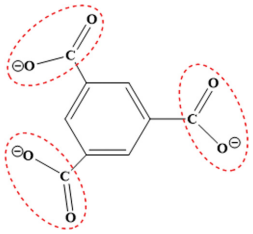
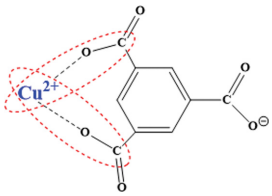
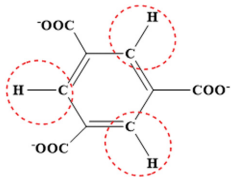
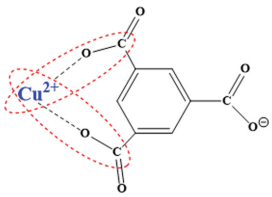
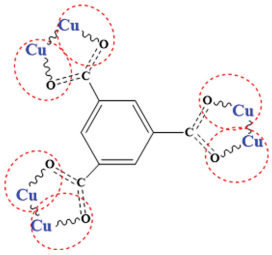
Wave numbers/cm^{-1}	Assignment	Source
3,700-3,000	O-H stretching vibration of bound water molecules	
3,427	O-H hydrogen-bonded stretching of HP-Cu-BTC surface	Adsorbed water
2,851/2,926	C-H stretching vibration	
2,349	Asymmetric stretching vibration of adsorbed CO_2	Adsorbed CO_2
1,632/1,580	O-C=O asymmetric stretching vibration of COO^- in BTC	
1,447/1,374	O-C=O symmetric stretching vibration of COO^- in BTC and/or silent symmetric stretching mode of adsorbed CO_2	
940/1,116	C-O-Cu stretching vibration	
1,040	C-H stretching vibration	
725/761	C-O-Cu stretching vibration	
489	Cu-O stretching vibration	

Table S3. Surface atomic concentrations of Cu^+ over HP-Cu-BTC

Adsorbent	Cu^+ ratio/%
Parent-Cu-BTC	4.21
HP-Cu-BTC(CTAB)	15.93
HP-Cu-BTC(N,N)	15.67
HP-Cu-BTC(SDBS)	18.17

ASAP 2020 HD88 Surface Area and Porosity Analyzer. Following each adsorption-desorption measurement at 273 K and 303 K at 0-100 kPa, the adsorbent is evacuated to less than 1 kPa to guarantee CO_2 adsorbed is recovered. The regenerated adsorbent was then utilized to quantify CO_2 adsorption-desorption.

Characterization

Cu^+ ration calculation results based on the peak areas in XPS spectra.

Gas Adsorption Analysis

To determine the CO_2/N_2 adsorption parameters of each metal-organic framework, CO_2 and N_2 isotherms were fitted using adsorption models. Basic adsorption models like the Langmuir with a single binding site, often fail to accurately characterize CO_2 adsorption on materials with strong binding sites. As such, the CO_2 adsorption on our metal-organic frameworks were described in this study using a dual-site Langmuir-Freundlich (DSLF) model.

$$q = q_1^{max} \times \frac{k_1 p^{1/n_1}}{1 + k_1 p^{1/n_1}} + q_2^{max} \frac{k_2 p^{1/n_2}}{1 + k_2 p^{1/n_2}} \quad (S1)$$

Here, q (mmol/g) is the quantity adsorbed, p (kPa) is the pressure, q_1^{max}, q_2^{max} (mmol/g) are the saturation workloads for sites 1 and 2, and k_1, k_2 (kPa^{-1}) are the Langmuir parameters for sites 1 and 2, respectively. The parameters n_1 and n_2 are utilized to determine the difference between the adsorbent and ideal surfaces. It is worth noting that when the heterogeneity parameter n_i=1, the DSLF model simplifies to the multisite Langmuir equation. On the other hand, the adsorption of N_2 is well represented by the Langmuir-Freundlich (SSLF) model.

$$q = \frac{q_m k_L p^{1/n}}{1 + k_L p^{1/n}} \quad (S2)$$

Where: q_m (mmol/g) is the single-site adsorption capacity per unit mass of the adsorbent, k_L (kPa^{-1}) is the Langmuir adsorption equilibrium constant, p (kPa) is the gas phase pressure at adsorption equilibrium, q (mmol/g) is the adsorption capacity, n is the surface heterogeneity parameter of the adsorbent.

By multiplying the remainder by the total of all the squares, the coefficient of determination R^2 was determined.

$$R^2 = 1 - \frac{\Sigma_{i=1}^{n} (y_i - f_{(x_i)})^2}{\Sigma_{i=1}^{n} (y_i - \bar{y})^2} \quad (S3)$$

y_i the i^{th} measured value, $f(x_i)$ the i^{th} linear equation value, and y is the average y value.

To achieve accurate values for the parameters, as an objective function, we utilize the average relative error (ARE/%), which is defined as follows:

$$ARE/\% = \frac{100}{N} \times \sum_{k=1}^{N} \left| \frac{q_{exp} - q_{cal}}{q_{exp}} \right| \quad (S4)$$

where q_{exp} and q_{cal} are the experimental and calculated data, N represents the total of data points, respectively.

Ideal adsorbed solution theory (IAST)

IAST is a powerful tool for forecasting gas mixture adsorption selectivities and equilibrium based on the isotherms of the single

Table S4. DSLF, SSLF isotherm parameters and average relative errors of pure CO_2 and N_2

Adsorbent/adsorbate	q_1 ($mmol \cdot g^{-1}$)	k_1 (kPa^{-1})	n_1	q_2 ($mmol \cdot g^{-1}$)	k_2 (kPa^{-1})	n_2	R^2	ARE/%
HP-Cu-BTC(CTAB)-CO_2-273 K	5.28539	0.01197	1.06018	5.28539	0.01197	1.06018	0.99968	3.209
HP-Cu-BTC(CTAB)-CO_2-298 K	7.01588	0.00363	1.02821	7.01588	0.00363	1.02821	0.99997	0.683
HP-Cu-BTC(CTAB)-CO_2-303 K	6.63476	0.00 323	1.00297	6.63476	0.00323	1.00297	0.99999	0.372
HP-Cu-BTC(CTAB)-N_2-273 K	4.85116	0.000748143	1.02757				1	0.161
HP-Cu-BTC(CTAB)-N_2-298 K	6.00143	0.000433396	1.00974				1	0.110
HP-Cu-BTC(CTAB)-N_2-303 K	5.37463	0.000418512	1.00473				1	7.633
HP-Cu-BTC(N,N)-CO_2-273 K	6.57775	0.00852	0.91632	6.57775	0.00852	0.91632	0.99998	1.913
HP-Cu-BTC(N,N)-CO_2-298 K	9.82687	0.00302	0.96505	9.82687	0.00302	0.96505	0.99999	0.629
HP-Cu-BTC(N,N)-CO_2-303 K	10.09691	0.00229	1.00084	10.09691	0.00229	1.00084	0.99998	0.381
HP-Cu-BTC(N,N)-N_2-273 K	8.07502	0.000567455	0.98548				0.99999	0.205
HP-Cu-BTC(N,N)-N_2-298 K	12.67403	0.000225332	0.98529				0.99999	0.137
HP-Cu-BTC(N,N)-N_2-303 K	25.09217	0.00010673	0.98239				0.99999	0.192
HP-Cu-BTC(SDBS)-CO_2-273 K	6.17285	0.01766	1.0795	6.17285	0.01766	1.0795	0.99982	2.114
HP-Cu-BTC(SDBS)-CO_2-298 K	6.53619	0.00367	0.95598	6.53619	0.00367	0.95598	0.99995	1.130
HP-Cu-BTC(SDBS)-CO_2-303 K	4.66473	0.00398	1.01869	4.66473	0.00398	1.01869	0.99998	0.561
HP-Cu-BTC(SDBS)-N_2-273 K	8.64363	0.000525693	1.02589				1	0.181
HP-Cu-BTC(SDBS)-N_2-298 K	11.01316	0.000261499	1.01574				1	0.178
HP-Cu-BTC(SDBS)-N_2-303 K	6.97638	0.000356929	1.0035				1	0.100

Table S5. CO_2 adsorption characteristics of Cu-BTC adsorbents in comparison to certain common Cu-BTC adsorbents

Adsorbent	T/K	P/kPa	CO_2 adsorption capacity	Ref.
Cu-BTC/GO	277	100	5.00	[2]
Cu-BTC/GO-U1	277	100	3.36	
Cu-BTC/GO-U2	277	100	4.89	
Cu-BTC/GO-U3	277	100	7.27	
Cu-BTC	295	100	3.08	[3]
CAU-1	273	100	7.2	[4]
	298	100	4.0	
Cu-BTC	298	1000	8.30	[5]
Cu-BTC@EDA	298	1000	6.45	
Cu-BTC@TETA	298	1000	5.50	
PANNF@MAC-H	298	2000	6.50	[6]
Cu-BTC	298	100	1.92	[7]
MWCNTs@Cu-BTC	298	100	3.26	
Imi1/3@Cu-BTC	298	100	4.4	[8]
HP-Cu-BTC(CTAB)	273	100	5.0699	This work
	298	100	3.4010	
	303	100	3.2064	
HP-Cu-BTC(N,N)	273	100	7.4293	
	298	100	5.1685	
	303	100	3.7509	
HP-Cu-BTC(SDBS)	273	100	6.8783	
	298	100	4.0798	
	303	100	2.4985	

components. IAST was used to predict CO_2/N_2 binary mixture adsorption in this paper. The adsorbed mixture, according to IAST, is the optimal spreading pressure and temperature solution, with the adsorbed solution's chemical potential equal to the gas phase's at equilibrium.

Myer and Prausnitz deduced the IAST by considering the adsorption phase to be a solution in symbiosis with the gaseous phase. As a result, it has a firm theoretical foundation for thermodynamics [9]. The IAST model is capable of performing numerical calculations simply, and the adsorption equilibrium of any multicomponent system may be estimated using just the data for pure components' adsorption equilibrium. As such, it is a well-established technique for forecasting multicomponent adsorption equilibrium models. From the Gibbs equation, the spreading pressure may be computed using the pure gas adsorption isotherm. The following is the equation.

$$\pi_i^0(p_i^0) = \frac{RT}{A}\int_0^{p_i^0} Q d\ln p \tag{S5}$$

where π is the adsorption diffusion pressure, p_i is the gas phase pressure when component i corresponds to the diffusion pressure π, R is the universal gas constant, and A is the specific surface area of the adsorbent. Under constant temperature conditions, the diffusion pressures of the single components remained the same. The equation is as follows:

$$\pi_1^0 = \pi_2^0 = \pi_0^3 = \cdots = \pi_n^0 = \pi \tag{S6}$$

For the binary adsorption of A and B, the IAST theory requires:

$$y_1 p_t = x_1 p_1 \tag{S7}$$

$$(1-y_1)p_t = (1-x_1)p_2 \tag{S8}$$

where y_1 and x_1 are the mole fractions of component 1 in the gas phase and the adsorption phase, respectively; P_t is the total pressure of the mixed gas, and P_1 and P_2 are the equilibrium pressures of pure components 1 and 2 in the adsorption phase, respectively.

Combination of DSLF and IAST Models

The DSLF-IAST model is expressed as follows [10,11]:

$$q_{c1}\ln\left(1+\frac{k_{c1}y_1 p^{(1/n_{c1})}}{x_1}\right)+q_{i1}\ln\left(1+\frac{k_{i1}y_1 p^{(1/n_{i1})}}{x_1}\right) - q_{c2}\ln\left(1+\frac{k_{c2}y_2 p^{(1/n_{c2})}}{1-x_1}\right)+q_{i2}\ln\left(1+\frac{k_{i2}y_2 p^{(1/n_{i2})}}{1-x_1}\right)=0 \tag{S9}$$

where q_{c1}, k_{c1}, q_{i1} and k_{i1} are the DSS model parameters of component 1; q_{c2}, k_{c2}, q_{i2} and k_{i2} are the DSS model parameters of component 2; y_2 is the mole fraction of component 2 in the gas phase; and x_2 is the mole fraction of component 2 in the adsorption phase. The unknown x_1 can be obtained using matrix laboratory (MATLAB) for fixed P_t and y_1 values.

The Total Adsorption Capacity of the Mixture

The total number of moles adsorbed (n_{total}) and each component adsorption capacity may be determined using the equation below:

$$\frac{1}{n_{total}} = \frac{x_1}{n_1(P_1^0)} + \frac{x_2}{n_2(P_2^0)} \tag{S10}$$

$$n_i = n_{total} x_i \quad (S11)$$

where, under given pressure conditions, n_{total} is the total molar adsorption capacity of the mixed gas, n_1 and n_2 are the adsorption capacities of single components 1 and 2 when the pressures are P_1 and P_2, respectively.

IAST selectivity:

The adsorption selectivity of HP-Cu-BTCs to CO_2/N_2 (15 vol% : 85 vol%) is calculated by the IAST model, and the calculation formula for selectivity is as follows:

$$S_{IAST} = \frac{x_1/x_2}{y_1/y_2} \quad (S12)$$

Among them, x_1 and x_2 represent the mole fractions of component 1 and component 2 in the adsorption phase, respectively. y_1 and y_2 are the mole fractions of component 1 and component 2 in the gas phase, respectively.

Adsorption selectivity on the basis of adsorption isotherm:

The adsorption selectivity (S_{ads}) of CO_2 over N_2 in HP-Cu-BTCs were derived from the data for the single-component isotherm. The calculation formula is as follows:

$$S_{ads} = \frac{q_{CO_2}/q_{N_2}}{P_{CO_2}/P_{N_2}} \quad (S13)$$

Where q_{CO_2} is the adsorbed quantity of CO_2 at 0.15 bar, q_{N_2} is the adsorbed quantity of N_2 at 0.85 bar.

Henry's law:

Equation for determining the CO_2/N_2 adsorption selectivities according to Henry's law constant is presented below:

$$K_H = \lim_{p \to 0} \frac{dq}{dp} \quad (S14)$$

where K_H is Henry's law constant, q is the adsorption uptake (mmol/g), and p is the gas pressure (kPa).

Selectivity according to Henry's law (upper limit selectivity) S_{Henry} can be expressed as follows:

$$S_{Henry} = \frac{K_i}{K_j} \quad (S15)$$

where K_i and K_j are Henry's law constant for components *i* and *j*, respectively.

Isosteric heat of adsorption (Q_{st}):

The Q_{st} of CO_2 adsorption, as a function of the quantity adsorbed were calculated using the CO_2 adsorption isotherms obtained at 273, 298, and 303 K. To determine this thermodynamic constant that represents the average interaction between adsorbent and adsorbate at a certain surface coverage. In this paper, the Q_{st} of adsorption is calculated by two types equations.

Firstly, Q_{st} was determined by fitting adsorption isotherm of the single-component at 273 K and 303 K using the Clausius-Clapeyron equation, which is illustrated below:

$$Q_{st} = -RT^2\left(\frac{\partial \ln P}{\partial T}\right)_q \quad (S16)$$

where Q_{st} (kJ·mol^{-1}) denotes the isosteric heat of adsorption at a particular adsorbent surface loading; R (kJ·mol^{-1}·K^{-1}) denotes to the universal gas constant, which is 8.3147×10^{-3} (kJ·mol^{-1}·K^{-1}); T (K) is the temperature; P (kPa) represents the pressure; q (mmol·g^{-1}) is the adsorbed amount. Integration of Eq. (S16) gives:

$$Q_{st} = \frac{-RT_1T_2}{T_2 - T_1}\ln\left(\frac{P_1}{P_2}\right) \quad (S17)$$

Then, we employed the virial-type equation, which has the following form [12-14]:

$$\ln(P) = \ln(n) + \left(\frac{1}{T}\right)\sum_{i=0}^{m} A_i n^i + \sum_{j=0}^{n} B_j n^j \quad (S18)$$

Among them, P (kPa) is the pressure, n (mmol·g^{-1}) is the adsorption capacity, T (K) is the temperature, both A_i and B_j are Virial constants, m and n represent the number of A_i and B_j, respectively, and R (kJ·mol^{-1}·K^{-1}) refers to the constant of universal gas, which is 8.3147×10^{-3} (kJ·mol^{-1}·K^{-1}).

The expression for calculating the heat of adsorption is as follows:

$$Q_{st} = -RT^2\left[\frac{\partial \ln P}{\partial T}\right]_N = R\sum_{i=0}^{m} A_i n^i \quad (S19)$$

Zero surface coverage: The initial Q_{st} is a critical metric for evaluating the adsorbate-adsorbent interactions. These values may be used to determine the most active adsorption site (such with unsaturated metal sites exposed or amine functional groups) and the force exerted by the adsorbents, and are often referred to as Q_{st} at zero coverage. It may be determined by extrapolating the virial graph's A_0 values:

$$Q_0 = -RA_0 \quad (S20)$$

Table S6. Henry's law constants and selectivity for HP-Cu-BTCs extrudates at 273, 298 and 303 K

Adsorbent	T/K	K_H (mmol·g^{-1}·kPa^{-1}) of CO_2	K_H (mmol·g^{-1}·kPa^{-1}) of N_2	S_{Herry}	S_{ads}	S_{IAST}
HP-Cu-BTC(CTAB)	273	0.07425	0.00332	22.364	30.834	33.29-34.24
	298	0.04999	0.00248	20.157	18.701	18.77-22.46
	303	0.04172	0.00212	19.679	19.058	18.83-20.07
HP-Cu-BTC(N,N)	273	0.12984	0.00415	31.287	26.511	28.85-37.18
	298	0.06448	0.00272	23.706	20.851	25.22-37.20
	303	0.04479	0.00246	18.207	15.533	15.77-18.44
HP-Cu-BTC(SDBS)	273	0.14968	0.00413	36.242	37.573	40.10-48.46
	298	0.05396	0.00272	19.838	19.424	18.12-22.29
	303	0.03541	0.00246	14.394	14.043	14.11-18.12

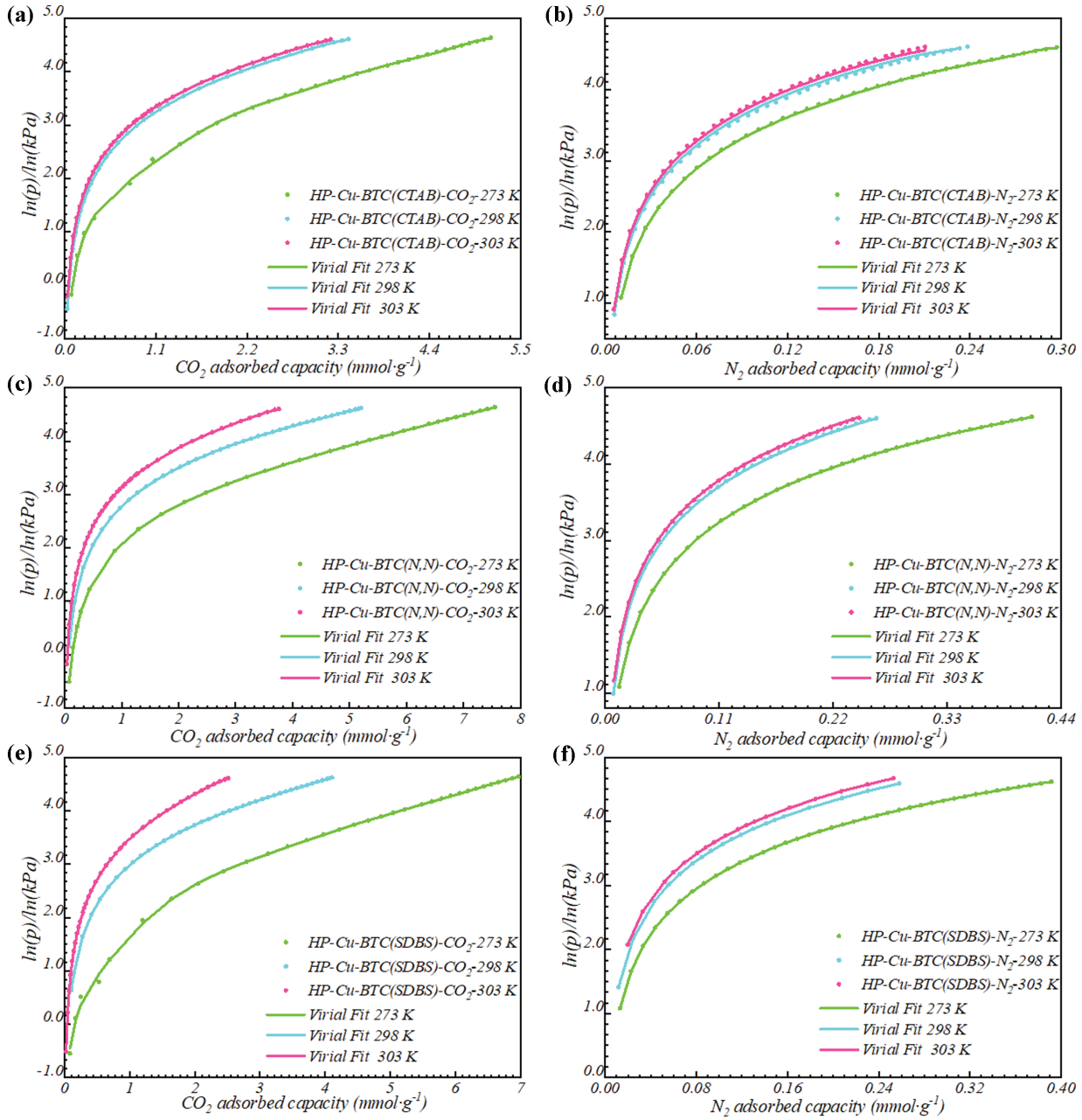


Fig. S5. Virial fitting curves of CO_2 (left) and N_2 (right) isotherms of (a), (b) HP-Cu-BTC(CTAB), (c), (d) HP-Cu-BTC(N,N) and (e), (f) HP-Cu-BTC(SDBS) at 273 (green), 298 (blue) and 303 K (pink).

A_0/ln(mmol·g^{-1}·kPa^{-1}) is related to the adsorbate-adsorbent interactions.

Fig. S6 show the Q_{st} of CO_2 and N_2 calculated by Clausius-Clapeyron equation utilizing a DSLF and SSLF adsorption model. The Q_{st} value reduces significantly with increasing CO_2 loading, owing to the availability of CO_2 molecules interact with unsaturated metal sites at low loading. The Q_{st} values for CO_2 adsorption loading on HP-Cu-BTC(N,N) range between 18.11 and 25.74 kJ/mol (<40 kJ· mol^{-1}), exhibiting high CO_2 physisorption interaction with unsaturated metal sites, but the relevant Q_{st} value is still significantly less than the chemical bond energy, promoting CO_2 desorption.

Kinetics of CO_2 Adsorption

To determine the rate of CO_2 adsorption on the three HP-Cu-BTCs adsorbents, their mass-transfer coefficients must be determined. Assume M g of adsorbent is abruptly introduced into a CO_2 flow. At time t>0, CO_2 adsorption occurred, and the quantity of CO_2 adsorbed on the adsorbent, q(t), grew with time. CO_2 adsorption was believed to have first-order kinetics, and the adsorption process was described using the following equation [15,16]:

$$\frac{\partial \overline{q}}{\partial t} = k_{eff}(q^* - q) \quad \text{(S21)}$$

where k_{eff} is the mass-transfer constant, q^* is the equilibrium quan-

Table S7. Virial equation parameters and correlation coefficients

Adsorbent	HP-Cu-BTC(CTAB)		HP-Cu-BTC(N,N)		HP-Cu-BTC(SDBS)	
Adsorbate	CO_2	N_2	CO_2	N_2	CO_2	N_2
A_0	−1,899.72488	−1,226.41886	−2,660.49691	−1,555.00234	−3,503.68512	−1,476.32637
A_1	−1,712.47021	6,119.08405	−607.94872	1,752.25283	−3,567.18186	2,122.87093
A_2	769.28386	−122,483.4205	344.77045	−47,188.50137	2,082.28179	−134,852.5717
A_3	340.66047	1,871,518.748	6.1918	715,458.2878	3.86439	3,094,995.905
A_4	−345.4797	−19,683000	−28.75724	−6,188,720.914	−239.79209	−35,458,000
A_5	116.44865	127,226,000	7.40199	31,549,700	76.87866	233,653,000
A_6	−22.01239	−472,711,000	−1.06191	−93,652,500	−12.99224	−899,314,000
A_7	2.20663	934,226,000	0.08029	149,589,000	1.12353	1,862,720,000
A_8	−0.09157	−759,895,000	−0.0025	−99,277,900	−0.03924	−1,600,940,000
B_0	9.31664	10.07045	11.77069	11.04095	14.80662	10.69974
B_1	6.45852	−13.23894	2.27302	−0.46939	12.2226	8.14696
B_2	−4.21347	119.37974	−1.45405	2.02138	−7.8563	−102.87777
B_3	0.76778	−367.72583	0.19582	−4.77717	1.24584	330.2659
R^2	0.9996	0.99886	0.99695	0.99995	0.99467	0.99979
ARE/%	0.821	0.054	0.148	0.189	0.0002	0.026
Q_0/(kJ·mol^{-1})	15.796	10.197	22.121	12.929	29.132	12.275

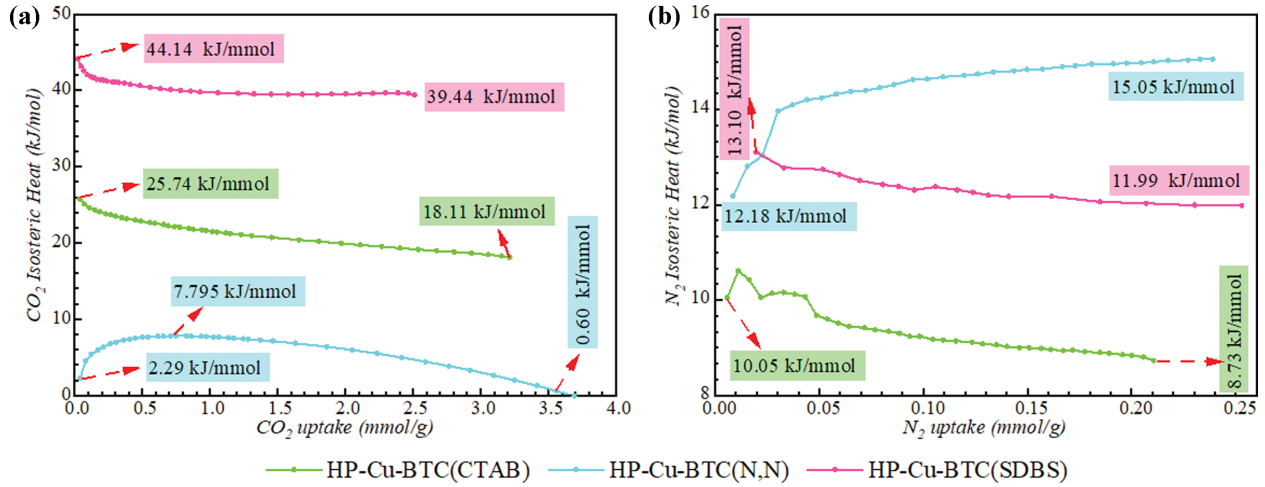


Fig. S6. Qst for (a) CO_2 and (b) N_2 on HP-Cu-BTCs calculated by Clausius-Clapeyron equation.

tity of CO_2 adsorbed at a given temperature, $q_{(t)}$ is the quantity of CO_2 absorbed by the adsorbent at time t, which may be measured using a gravimetric approach. The integral equation was as follows from Eq. (S20).

$$q_t = q_e(1-e^{-k_{eff}t}) \tag{S22}$$

To determine the correctness of the Pseudo-first-order model, the dimensionless standard deviation of the model is calculated using an error function based on the dimensionless standard deviation. The following is the expression:

$$\sigma\% = \sqrt{\frac{1}{N}\sum_{1}^{N}\left(\frac{q_{exp}-q_{cal}}{q_{exp}}\right)^2} \tag{S23}$$

Where σ% is the dimensionless standard deviation, q_{exp} and q_{cal} are the experimentally measured adsorption capacity and the calculated adsorption capacity calculated according to the model, and N represents the number of experimental data points.

The second-order model is based on the premise that the rate of adsorption is proportional to the square of the number of available adsorption sites. The rate of adsorption may be represented as follows [17]:

$$\frac{\partial \overline{q}}{\partial t} = k_{eff}(q^* - q)^2 \tag{S24}$$

From Eq. (S24), the integral equation was available as follows:

$$q_t = \frac{q_e^2 k_{eff} t}{1 + q_e k_{eff} t} \tag{S25}$$

If the adsorbent has a highly developed porous structure or a pore structure that is mostly made of micropores, the adsorbent's CO_2 adsorption process may be evaluated by the diffusion resis-

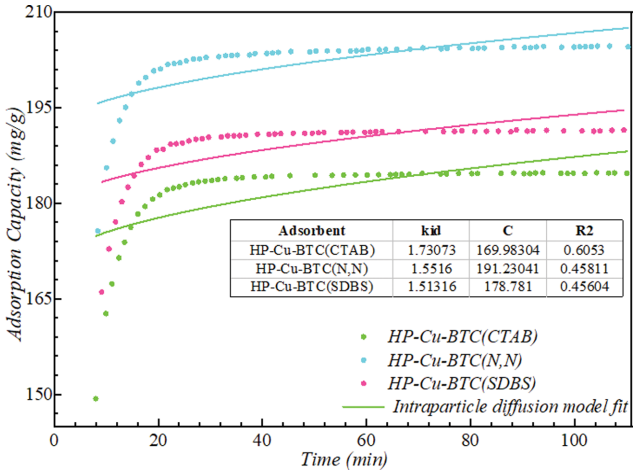


Fig. S7. Adsorption kinetics curves of CO_2 on the HP-Cu-BTC(CTAB)-green, HP-Cu-BTC(N,N)-blue and HP-Cu-BTC(SDBS)-pink at 298 K and 100 kPa. Solid lines correspond to fits to the CO_2 data employing Intraparticle diffusion model.

tance between particles, that is, the diffusion resistance in the pores. Weber-Morris [18] presented an inter-particle diffusion model to explain the adsorption process dictated by diffusion in the pores in accordance with Fick's second law of diffusion. The interparticle diffusion model is a simplified representation of pore diffusion kinetics.

$$q_t = k_{id} t^{1/2} + C \tag{S26}$$

Where k_{id} (mol/kg·min$^{0.5}$) is the diffusion rate constant between particles, and C is the intercept, which represents the thickness of the boundary layer.

Adsorption Capacity:

The adsorption period (t), the input flow rate of the particular gas (F_{in}), the exit flow rate of the specific gas (F_{out}), the dead volume of the adsorption system (V_{dead}), and the mass of the adsorbent (m) may be used to determine the quantity of adsorbed gas (q):

$$q = \frac{F_{in} \cdot t - V_{dead} - \int_0^t F_{out} dt}{m} \tag{S27}$$

Separation Rate of CO_2 to N_2

A simple equation can be used to figure out the CO_2/N_2 selectivity. In this equation, y is the mole fraction of a gas in the feed gas stream:

$$S = \frac{q_{CO_2}/q_{N_2}}{y_{CO_2}/y_{N_2}} \tag{S28}$$

It goes without saying that such measurements should always be conducted in circumstances that are as near to those encountered during CO_2 collection from flue gas as feasible, particularly in terms of temperature/pressure and the presence of H_2O and O_2.

Diffusion Coefficient:

$$D = \frac{L^2}{6t_{eq}} \tag{S29}$$

Formula D (cm^2/s) is the effective diffusion coefficient; L (cm) is the loading length, namely, the thickness of the fixed bed layer; t_{eq} (s) is the delay time, namely, the abscess of the extension line of the steady flow line in the outflow curve and the focus of the X-axis minus the outflow time.

The outflow time is the time from the beginning of adsorption penetration to the outflow of adsorbent gas through the column.

Taking CO_2 out of the flue gas has become more important because of how important it is to the environment. Because HP-Cu-BTCs exhibit excellent CO_2 adsorption capacity, regenerability, and a low and relatively constant isosteric heat of CO_2 adsorption, their selectivities for CO_2 adsorption over N_2 are critical factors to consider when evaluating the feasibility of using this material as a CO_2 separation medium in real-world applications. The breakthrough readings are significantly more in line with real gas purification operations, and numerous examples demonstrate that the selectivity

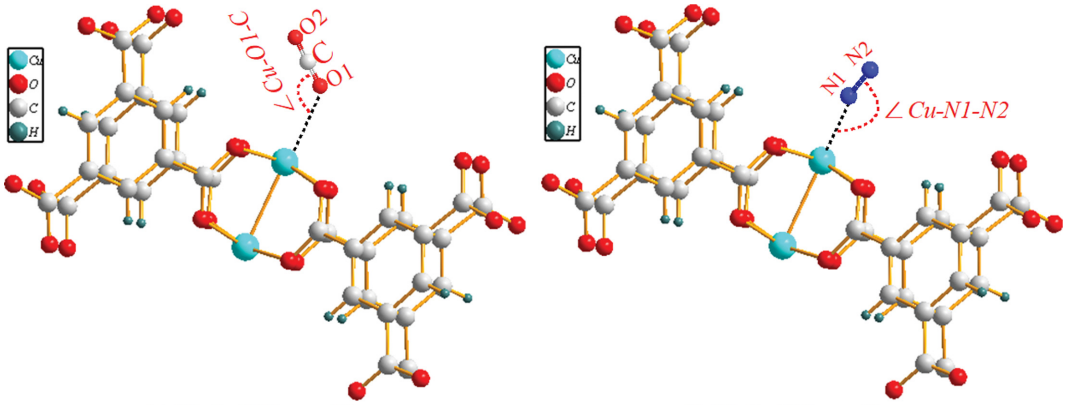
Table S8. Kinetics Parameters and Standard deviation of CO_2 on HP-Cu-BTCs at 298 K and 100 kPa

Adsorbent	q_{exp}	q_{cal}	k_{eff} (1/min)	Standard deviation/%
HP-Cu-BTC(CTAB)	184.71445	184.4394	0.20699	1.96173E-05
HP-Cu-BTC(N,N)	204.57275	203.9901	0.22212	6.58168E-05
HP-Cu-BTC(SDBS)	191.49445	191.0728	0.21568	1.74056E-05

Table S9. Kinetic selectivity and Diffusion Coefficient of CO_2 on HP-Cu-BTCs at 298 K and 1 atm

Adsorbent	Adsorbate	Saturated adsorption capacity (cm^3/g)	Kinetic selectivity	Outflow time/(s)	Delay time	Bed thickness	Diffusion coefficient/(cm^2/s)
HP-Cu-BTC(CTAB)	CO_2	13.289	7.6296	301.96	1,340.07	8.5	0.0090
	N_2	9.870		147.27	67.26	8.5	0.1790
HP-Cu-BTC(N,N)	CO_2	14.534	7.4831	679.14	910.21	8.5	0.0132
	N_2	11.006		185.41	28.15	8.5	0.4278
HP-Cu-BTC(SDBS)	CO_2	13.665	8.8014	509.62	1,380.71	7.5	0.0068
	N_2	8.798		168.46	46.36	7.5	0.2022

The outflow time is the time from the beginning of adsorption penetration to the outflow of adsorbent gas through the column.



(a) HP-Cu-BTC·····CO_2 (b) HP-Cu-BTC·····N_2

Fig. S8. The architectures of molecules adsorbing on the open Cu sites of neutral Cu-BTC are (a) CO_2 and (b) N_2. The unit of measurement for distance is Å.

Table S10. The calculated adsorption energies (E_{ads}) and geometric parameters of the X…Cu-BTC (X=CO_2 and N_2) adducts, including the Cu…X ($d_{Cu...X}$) distance, Cu-Cu bond length ($d_{Cu...Cu}$), intramolecular bond lengths of the guest molecules in adsorption adducts ($d1_{X1-X2}$) and gas phase ($d2_{X1-X2}$). Note that X1-X2 in CO_2 and N_2 stand for the O1-C and N1-N2 bonds, respectively

Adsorbent-adsorbate		E_{ads} (eV)	$d_{Cu...X}$ (Å)	$d_{Cu...Cu}$ (Å)	∠Cu-X1-X2 (°)	$d1_{X1-X2}$ (Å)	$d2_{X1-X2}$ (Å)
Cu-BTC	GGA	-	-	2.46	-	-	-
	LDA	-	-	2.41	-	-	-
HP-Cu-BTCs…CO_2	GGA	0.13	2.49	2.47	110	1.18	1.18
	LDA	0.32	2.49	2.42	117	1.17	1.17
HP-Cu-BTCs…N_2	GGA	0.11	2.36	2.48	172	1.11	1.11
	LDA	0.32	2.15	2.45	175	1.10	1.10

LDA stands for local density approximation, while GGA stands for generalized gradient approximation computations.

predicted by IAST may be more accurate for selectivity in real mixed-gas separation [19,20]. Moreover, a volumetric adsorption device is unable to assess regenerability/cycle stability; however, mixed gas breakthrough makes this information available.

REFERENCES

1. C. Duan, F. Li, H. Zhang, J. Li, X Wang and H. Xi, *RSC Adv.*, **7**, 52245 (2017).
2. A. Policicchio, Y. Zhao, Q. Zhong, R. G. Agostino and T. J. Bandosz, *ACS Appl. Mater. Interfaces*, **6**, 101 (2014).
3. J. Xie, N. Yan, Z. Qu and S. Yang, *J. Energy Environ. Sci.*, **24**, 640 (2012).
4. X. Si, C. Jiao, F. Li, J. Zhang, S. Wang, S. Liu, Z. Li, L. Sun, F. Xu, Z. Gabelica and C. Schick, *Energy Environ. Sci.*, **4**, 4522 (2011).
5. S. Salehi, M. Anbia and F. Razavi, *Environ. Prog. Sustain. Energy*, **39**, 13302 (2020).
6. M. Tajer, M. Anbia and S. Salehi, *Environ. Prog. Sustain. Energy*, **40**, e13498 (2021).
7. S. Ullah, A. M. Shariff, M. A. Bustam, A. E. I. Elkhalifah, G. Gonfa and F. A. A. Kareem, *J. Chin. Chem. Soc.*, **63**, 1022 (2016).
8. H. Li, Z. Lin, X. Zhou, X. Wang, Y. Li, H. Wang and Z. Li, *Chem. Eng. J.*, **307**, 537 (2017).
9. A. L. Myers and J. M. Prausnitz, *AIChE J.*, **11**, 121 (1965).
10. A. Tarafder and M. Mazzotti, *Chem. Eng. Technol.*, **35**, 102 (2012).
11. F. R. Siperstein and A. L. Myers, *AIChE J.*, **47**, 1141 (2001).
12. L. Czepirski and J. Jagiełło, *Chem. Eng. Sci.*, **44**, 797 (1989).
13. D. Britt, H. Furukawa and B. Wang, *Proc. Natl. Acad. Sci.*, **106**, 20637 (2009).
14. J. L. C. Rowsell and O. M. Yaghi, *J. Am. Chem. Soc.*, **128**, 1304 (2006).
15. J. M. Borah, J. Sarma and S. Mahiuddin, *Colloids Surf. A Physicochem. Eng. Asp.*, **387**, 50 (2011).
16. R. Serna-Guerrero and A. Sayari, *Chem. Eng. J.*, **161**, 182 (2010).
17. Y. S. Ho and G. McKay, *Can. J. Chem. Eng.*, **76**, 822 (2010).
18. J. C Morris and W. J. Weber, *J. R. Adv. Water. Resour.*, **269**, 231 (1964).
19. Y. Zhao, K. X. Yao, B. Teng, T. Zhang and Y. Han, *Energy Environ. Sci.*, **6**, 3684 (2013).
20. P. Nugent, Y. Belmabkhout, S. D. Burd, A. J. Cairns, R. Luebke, K. Forrest, T. Pham, S. Ma, B. Space, L. Wojtas, M. Eddaoudi and M. J. Zaworotko, *Nature*, **495**, 80 (2013).